Development of Mist-Based Technologies for Droplet-based and Coaxial Bioprinting of Ionically Crosslinking Hydrogels

by

Sara BADR

THESIS PRESENTED TO ÉCOLE DE TECHNOLOGIE SUPÉRIEURE IN PARTIAL FULFILLEMENT FOR A MASTER'S DEGREE WITH THESIS IN MECHANICAL ENGINEERING
M.A.Sc.

MONTREAL, APRIL 28, 2023

ÉCOLE DE TECHNOLOGIE SUPÉRIEURE
UNIVERSITÉ DU QUÉBEC

BOARD OF EXAMINERS

THIS THESIS HAS BEEN EVALUATED

BY THE FOLLOWING BOARD OF EXAMINERS

Mr. Ali Ahmadi, Thesis Supervisor
Department of Mechanical Engineering, École de technologie supérieure

Mr. Lucas Hof, President of the Board of Examiners
Department of Mechanical Engineering, École de technologie supérieure

Mr. Giuseppe Di Labbio, Member of the jury
Department of Mechanical Engineering, École de technologie supérieure

THIS THESIS WAS PRENSENTED AND DEFENDED

IN THE PRESENCE OF A BOARD OF EXAMINERS AND PUBLIC

APRIL 4, 2023

AT ÉCOLE DE TECHNOLOGIE SUPÉRIEURE

DEDICATION

To my parents, Maram and Walid,
for everything they have done to help me get where I am today.

ACKNOWLEDGMENT

First and foremost, I would like to express my deepest and sincerest gratitude to my supervisor, Dr. Ali Ahmadi, for his continuous guidance, support, and encouragement throughout my research journey. Your expertise and mentorship have been instrumental in shaping my research and helping me to achieve my goals. I would also like to thank Dr. Andrew Tasker at the Department of Biomedical Sciences, University of Prince Edward Island for his guidance and invaluable feedback throughout my master's program.

I would like to extend my special thanks to my lab mates; I greatly appreciate the friendly environment I was surrounded with during my time in the lab. I would specifically like to acknowledge Ben MacCallum, my co-first author, for his contributions to the droplet-based bioprinting project; he conducted the preliminary optimization tests, contributed to manuscript writing and editing, and conducted simulation analysis. I would also like to thank Debra MacDonald for training me on cell culture in Dr. Tasker's lab at the University of Prince Edward Island.

My most profound appreciation goes to my family and friends for their endless love and support. I am deeply grateful to each and every one who has played a role in making this journey a memorable and successful one. I could not have without the support provided, and I will always cherish their contributions to my life and academic pursuits.

Lastly, I would like to acknowledge the funding that supported this research including Natural Sciences and Engineering Research Council of Canada (NSERC), Canada Graduate Scholarships – Master's program (CGS M).

Développement de la technologie de brumisateur pour la bio-impression de gouttelettes et coaxiale

Sara BADR

RÉSUMÉ

La bio-impression tridimensionnelle est devenue l'une des majeures techniques de biofabrication pour la fabrication de tissus, permettant une précision et une résolution élevées du dépôt de l'encre. Les hydrogels à réticulation ionique sont parmi les plus couramment utilisés dans la bio-impression tridimensionnelle en raison de leur biocompatibilité, de leur facilité de réticulation et de leur gélification rapide. Les méthodes actuelles de bio-impression d'hydrogels à réticulation ionique reposent sur l'utilisation d'un agent de réticulation liquide, qui empêche un dépôt précis des encres et entraîne une mauvaise résolution et une mauvaise adhésion des couches. En outre, les approches actuelles impliquent de multiples étapes de réticulation et de post-traitement, ce qui prend du temps et pourrait compromettre la fidélité de la forme de la structure imprimée et la viabilité des cellules. Par conséquent, un système amélioré permettant de mieux contrôler le taux de gélification et de collecter l'excès d'agent réticulant sous forme de brumisateur doit être développé.

Dans cette thèse, des technologies basées sur le brumisateur sont développées pour la bio-impression tridimensionnelle d'encres d'hydrogel à réticulation ionique. La technique de réticulation par brumisateur est mise en œuvre pour deux techniques de bio-impression, la bio-impression par gouttelettes et la bio-impression coaxiale. Contrairement aux approches actuelles de la bioimpression par gouttelettes et coaxiale qui utilisent l'agent de réticulation sous forme liquide ou sacrificielle pour construire un échafaudage, les technologies développées introduisent l'agent de réticulation sous forme de brumisateur.

Pour l'étude de la bio-impression à base de gouttelettes, la tête d'impression introduit l'agent de réticulation sous forme de brumisateur et comporte un mécanisme d'élimination qui empêche l'accumulation de l'agent de réticulation sur le lit d'impression. Il est démontré que le taux de gélification peut être contrôlé en ajustant le taux de distribution du brumisateur. En conséquence, il est démontré que le taux de distribution du brumisateur a un impact sur la fidélité de la forme et les propriétés mécaniques des constructions imprimées. L'imprimabilité et les propriétés de gonflement des constructions imprimées réticulées en utilisant différents taux de distribution du brumisateur sont étudiées. De plus, les impacts des paramètres d'impression, y compris la hauteur de la tête d'impression, la pression de sortie du brumisateur et les dimensions du canal de la tête d'impression sur la distribution du brumisateur et, par conséquent, sur le taux de gélification dans la tête d'impression, sont étudiés. De plus, en utilisant l'imagerie à haute vitesse, les effets de la concentration du brumisateur et de la vitesse des gouttelettes sur la dynamique de l'impact des gouttelettes sur la surface sont caractérisés. Les résultats montrent que les constructions imprimées à l'aide de la tête d'impression développée présentent une bonne gélification des gouttelettes et une bonne adhésion des co-gouttelettes, ainsi qu'un niveau élevé de viabilité cellulaire.

Pour l'étude de la bio-impression coaxiale, la technologie à base de brumisateur est évaluée pour la fabrication de fibres creuses en une seule étape. Grâce à l'exposition contrôlée de l'agent de réticulation, le système développé évite une mauvaise résolution et une mauvaise adhésion des couches causées par l'accumulation d'agent de réticulation liquide sur le lit d'impression. En outre, il élimine les étapes de traitement supplémentaires, telles que la réticulation partielle de l'hydrogel avant ou l'élimination du matériau sacrificiel après l'impression. L'imprimabilité et les propriétés mécaniques des échafaudages de fibres creuses imprimés en utilisant différentes concentrations de brumisateur et d'hydrogel sont étudiées. Il est démontré que la concentration du brumisateur influence le taux de gélification de la fibre creuse, ce qui a un impact sur la fidélité de la forme, l'adhésion des couches et les propriétés mécaniques des structures imprimées. De plus, les effets des paramètres d'impression, y compris la pression du noyau du brumisateur et le débit de l'hydrogel, sur le diamètre et l'épaisseur de la paroi de la fibre creuse sont étudiés. En outre, les échafaudages imprimés et réticulés à l'aide du brumisateur présentent une viabilité cellulaire supérieure à 90 %. Le système coaxial à base de brumisateur développé permet l'impression directe de fibres creuses continues.

La technologie de réticulation basée sur le brumisateur exploite les avantages des techniques de bio-impression, tout en offrant un meilleur contrôle de la vitesse de gélification et en empêchant l'accumulation d'un excès de réticulant sur le lit d'impression. En outre, les technologies développées basées sur le brumisateur font progresser l'applicabilité de la bio-impression basée sur les gouttelettes et coaxiale pour fabriquer des échafaudages complexes et biocompatibles pour les applications d'ingénierie tissulaire.

Mots-clés : Bio-impression 3D, à base de gouttelettes, coaxiale, brumisateur, alginate, fibre creuse

Development of mist-based technologies for droplet-based and coaxial bioprinting of ionically crosslinking hydrogels

Sara BADR

ABSTRACT

Three-dimensional bioprinting has become one of the leading biofabrication techniques in the pursuit of creating tissue constructs, as it offers high precision and resolution of bioink deposition. Ionically crosslinking hydrogels are one of the most commonly used in three-dimensional bioprinting due to their biocompatibility, ease of crosslinking, and rapid gelation. Current methods of bioprinting ionically crosslinking hydrogel bioinks rely on the use of liquid crosslinker, which impedes precise deposition of the bioinks and causes poor resolution and layer adhesion. Furthermore, current approaches involve multiple crosslinking stages and post-processing steps, which is time consuming and could compromise the shape fidelity of the printed structure and cell viability. Therefore, an improved system to better control the gelation rate and collect the excess mist crosslinker must be developed.

In this thesis, mist-based technologies are developed for the three-dimensional bioprinting of ionically crosslinking hydrogel bioinks. The mist-based crosslinking technique is implemented for two bioprinting techniques, droplet-based and coaxial bioprinting. Contrary to current approaches to droplet-based and coaxial bioprinting that utilize the crosslinker in liquid or sacrificial form to construct a scaffold, the developed technologies introduce the crosslinking agent in mist form.

For the droplet-based bioprinting study, the printhead introduces the crosslinker in mist form, and features a removal mechanism that prevents crosslinker accumulation on the printbed. It is shown that the gelation rate can be controlled by adjusting the mist concentration or delivery rate. Furthermore, it is shown that the mist inlet flowrate has influences on the printing resolution and shape fidelity of the printed constructs. The printability, mechanical properties, and swelling properties of the printed constructs crosslinked using different mist delivery rates are studied. Moreover, the impacts of printing parameters, including printhead height, mist outlet pressure and printhead channel dimensions on the mist distribution within the printhead is investigated. Additionally, using high-speed imaging, the effects of mist concentration and droplet velocity on the dynamics of droplet impact onto the printing surface are characterized. Results show that the printed constructs using the developed printhead exhibit good droplet gelation and co-droplet adhesion, and high level of cell viability.

For the coaxial bioprinting study, the mist-based technology is evaluated for fabricating hollow fibers in a single step. Through controlled exposure of crosslinker, the developed system prevents poor resolution and layer adhesion caused by the accumulation of liquid crosslinker on the printbed. Furthermore, it eliminates additional processing steps, such as partial crosslinking of the hydrogel prior- or removal of sacrificial material post-printing. The printability and mechanical properties of hollow fiber scaffolds printed using various mist and hydrogel concentrations are studied. It is shown that mist concentration influences the gelation

rate of the hollow fiber, impacting the shape fidelity, layer adhesion, and mechanical properties of the printed structures. Moreover, the effects of printing parameters, including the mist core pressure and hydrogel flowrate, on the diameter and wall thickness of the hollow fiber are investigated. Additionally, scaffolds printed and crosslinked using mist exhibit over 90% cell viability. The developed mist-based coaxial system enables direct printing of continuous hollow fibers.

The developed mist-based crosslinking technology leverages the advantages of bioprinting techniques, while providing a better control of the gelation rate and preventing the accumulation of excess crosslinker on the printbed. Furthermore, the developed mist-based technologies advance the applicability of droplet-based and coaxial bioprinting to fabricate complex and biocompatible scaffolds for tissue engineering applications.

Keywords: 3D bioprinting, droplet-based, coaxial, mist-based, calcium alginate, hollow fiber

PREFACE

The present thesis is based on the work conducted in the Atlantic Biofabrication Lab at the University of Prince Edward Island, as well as the Biomaterials and BioFabrication Lab (BBF) at the University of Montreal Hospital Research Centre (CRCHUM) and École de technologie supérieure (ÉTS).

The content of this thesis is under consideration for publication or have already been published in scientific journals. Chapter 3, the development of mist-based printhead for droplet-based bioprinting of ionically crosslinking hydrogels, is published in *Bioprinting*. Ben MacCallum is a co-first author on this paper, he conducted the preliminary optimization tests, flow simulation analysis, and contributed to the manuscript writing and editing. Elias Madadian and Emad Naseri conducted the droplet impact analysis and compression/rheology tests, respectively. The mist-based method for coaxial bioprinting of ionically crosslinking hydrogels presented in Chapter 4 is under consideration for publication in a journal and has been published in one conference proceeding. Elias Madadian assisted in performing the cell viability experiments.

Peer-reviewed journal articles

1. **Badr, S.,** Madadian, E., Naseri, E., Wheatley, S. K., & Ahmadi, A. (2023). A review on biofabrication techniques of hollow fibers, *Biofabrication* (Under preparation).
2. **Badr, S.,** Madadian, E., MacDonald, D., Tasker, R.A., & Ahmadi, A. (2023). A mist-based crosslinking technique for coaxial bioprinting of hollow hydrogel fibers, *Bioprinting* (Submitted).
3. **Badr, S.,** MacCallum, B., Madadian, E., Kerr, G., Naseri, E., MacDonald, D., Tasker, R.A., & Ahmadi, A. (2022). Development of a mist-based printhead for droplet-based bioprinting of ionically crosslinking hydrogel bioinks. Bioprinting, 27, e00207. ***Contributions:*** S. Badr and B. MaCallum contributed equally to this work.
4. Madadian, E., **Badr, S**., MacDonald, D., Tasker, R.A. & Ahmadi, A. (2023). Development of a foam-based method for coaxial bioprinting of ionically crosslinking bioinks, *Bioprinting* (Under Review).

Contributions: S. Badr and E. Madadian performed the mechanical, cell viability, and diameter and wall thickness tests. S. Badr analyzed the mechanical and wall diameter and thickness results. S. Badr drafted the cell viability section of the manuscript.

5. Wheatley, S. K., Cartmell, C., Madadian, E., **Badr, S**., Haltli, B. A., Kerr, R. G., & Ahmadi, A. (2022). Microfabrication of a micron-scale microbial-domestication pod for in situ cultivation of marine bacteria. RSC advances, 12(43), 28123-28127. ***Contributions:*** S. Badr performed the printability analysis of the micron-scale microbial domestication pod.

Conference presentations and proceedings

1. **Badr, S**., Madadian, E., MacCallum, B., Naseri, E., MacDonald, D., Tasker, R.A., & Ahmadi, A. Development of a mist-based printhead technology for extrusion-based, droplet-based and coaxial bioprinting, The 26th International Conference on Miniaturized systems for Chemistry and Life Sciences (MicroTAS 2022), Hanghzhou, China. Abstract and oral presentation.
2. Madadian, E., **Badr, S**., MacDonald, D., Tasker, R.A., & Ahmadi, A. Development of a foam-based method for coaxial bioprinting of ionically crosslinking bioinks. International Conference on Biofabrication (2022), Pisa, Italy. Abstract and oral presentation.
3. **Badr, S**., MacCallum, B., Madadian, E., Naseri, E., MacDonald, Bodaghkhani, A., D., Tasker, R.A., & Ahmadi, A. Development of a mist-based printhead technology for extrusion-based, droplet-based and coaxial bioprinting, International Conference on Biofabrication (2021), Australia. Abstract and poster presentation.
4. Madadian, E., **Badr, S**., & Ahmadi, A. Investigation of impact dynamics of ionically crosslinking hydrogel droplets in mist-based 3D bioprinting applications. Proceedings of the Canadian Society for Mechanical Engineering International Congress (CSME 2021), Prince Edward Island, Canada. Abstract and oral presentation.

TABLE OF CONTENTS

Page

LIST OF TABLES

Page

LIST OF FIGURES

Page

LIST OF ABREVIATIONS

3D	three-dimensional
ANOVA	analysis of variance
EBB	extrusion-based bioprinting
ECM	extracellular matrix
DAPI	4’6-diamidino-2-phenylindole dihydrochloride
DBB	droplet-based bioprinting
PBS	phosphate-buffered saline
PI	propidium iodide
PR	Printability number
RGD	Arg-Gly-Asp
SR	swelling ratio
TE	tissue engineering
UV	ultraviolet

LIST OF SYMBOLS AND UNITS OF MEASUREMENTS

a	radius of the droplet (μm)
ε	strain
C	concentration of the crosslinker ions within the bioink droplet
C_c	concentration at the center of the droplet
C_s	crosslinker concentration at the surface of the bioink droplet
D_c	diffusion coefficient of crosslinker ions m^2/s
D_i	initial diameter of the droplet (μm)
$D(t)$	diameter (μm) of the droplet at time, t
L_i	initial length (mm)
L_f	final length (mm)
r	radial distance (m)
t	time (s)

INTRODUCTION

Tissue engineering plays an exceptionally important role in addressing the ongoing organ shortage crisis (Vacanti, 1993). Three-dimensional bioprinting (3D) is one of the most promising techniques in tissue engineering, as it allows for precise control over the structure and composition of the tissue construct (Hospodiuk, Dey, Sosnoski, & Ozbolat, 2017)(Agarwal et al., 2020). 3D bioprinting allows the creation of tissue constructs that closely mimic the microarchitecture, mechanical properties, and cellular organization of native tissues (Jain, Kathuria, & Dubey, 2022)(Datta, Ayan, & Ozbolat, 2017)(Ahadian & Khademhosseini, 2018). In 3D bioprinting, a cell-laden biomaterial, known as bioink, is deposited on substrate in a layer-by-layer fashion to create tissue-like structures upon crosslinking (Hospodiuk et al., 2017)(Chung et al., 2013)(Karamchand et al., 2023). Hydrogels are among the most common biomaterials used in bioprinting due to their biocompatibility and high-water absorbing properties, and ability to closely mimic cellular microenvironments (Karamchand et al., 2023)(Hull, Brunel, & Heilshorn, 2022).

Hydrogels undergo a crosslinking process to form a printable solid gel (Karamchand et al., 2023). There are various gelation mechanisms including thermal (Wüst, Godla, Müller, & Hofmann, 2014), ionic (Aguero, Alpdagtas, Ilhan, Zaldivar-Silva, & Gunduz, 2021), photo (Zennifer, Manivannan, Sethuraman, Kumbar, & Sundaramurthi, 2021), pH (Sarrigiannidis et al., 2021), and enzymatic (de Melo et al., 2020) crosslinking. Among these, ionically crosslinking hydrogels are one of the most commonly used due to their ease of crosslinking and rapid gelation kinetics (F. Xu et al., 2022). However, the low viscosity and rapid crosslinking of the hydrogel precursors can pose challenges when printing using conventional, liquid-based crosslinking methods. Several strategies have been developed to enable ionically crosslinking hydrogel bioprinting; however, they suffer from poor shape fidelity, poor layer adhesion, and diminished cell viability. Therefore, an improved method of crosslinking hydrogel bioinks must be developed.

The aim of this thesis is to explore the potential/investigate the suitability of mist-based technologies for droplet-based and coaxial bioprinting of ionically crosslinking hydrogels. The present thesis consists of four chapters. Chapter 1 provides a brief literature review on three-dimensional bioprinting and the current methods and strategies of fabricating ionically crosslinking hydrogels along with their limitations. The specific objectives of the thesis are also discussed.

Chapter 2 focuses on the theory and experimental methods used throughout the thesis. The theory behind the diffusion of crosslinker ions into hydrogel precursor is included. The experimental work includes the 3D bioprinting setup, printability analysis, flow simulation of mist distribution within the printhead, the measurement of hollow fiber dimensions , rheological and mechanical characterization, swelling tests, and cell viability tests.

The results of development of mist-based printhead for droplet-based bioprinting (DBB) of ionically crosslinking hydrogels are presented and discussed in Chapter 3. The impacts of printing parameters on the mist distribution within the printhead is investigated using flow simulation. The rheological properties, printability, mechanical characterization, and swelling properties of the printed constructs are presented. It is shown that the mist delivery rate has an impact on the crosslinking rate, and thus, affects the shape fidelity, co-droplet and layer adhesion, and mechanical properties of the printed constructs. Finally, the biocompatibility of the printed constructs with neuron cells is studied.

The results of the development of mist-based method for coaxial bioprinting are presented and discussed in Chapter 4. The suitability of mist-based crosslinking for coaxial bioprinting is investigated. The printability analysis, dimension measurements, mechanical properties, and biocompatibility of the printed hollow fibers constructs are presented. The effects of the core pressure and sheath flowrate on the uniformity, diameter, and wall thickness of the hollow fibers are studied. Furthermore, it is shown that the mist concentration has an impact on the printability and mechanical properties of the printed hollow fiber scaffolds, and the crosslinking rate can be controlled by adjusting the mist concentration, thus improving the

layer adhesion and printability of the printed structures. Additionally, results indicate that the mist-based crosslinking technique does not influence the viability of neuron cells. The thesis concludes with a summary of the results, highlights of the work presented, and recommended future research directions.

CHAPTER 1

LITERATURE REVIEW

1.1 Tissue engineering

Organ shortage is a persistent and ongoing critical issue that majorly affects people worldwide. The increased demand for organ transplantation and limited availability of adequate organ transplants has created a severe shortage crisis. Unfortunately, the organ shortage has resulted in millions of people worldwide waiting years to receive life-saving transplants. In the United States (U.S.) alone, over 100,000 people are waiting for an organ transplant, with an average wait time of approximately five years. However, only about 40% of people in need of an organ transplant will receive one. Additionally, approximately 20 people die every day in the U.S. while waiting for a transplant. This information is taken from the United Network for Organ Sharing (UNOS) website (https://unos.org/).

Over the past few decades, tissue engineering, which was first officially introduced at a National Science Foundation workshop in 1988 (O'Brien, 2011), has emerged as a promising approach to address the increasing demand for tissue and organ replacements/alleviate the organ shortage crisis (Vacanti, 1993). Tissue engineering is a rapidly growing interdisciplinary field that applies the principles of biological sciences and engineering to develop/produce biological constructs to restore, maintain, or enhance the structures and functions of tissue due to damage, injury, or disease through the use of cells, biomaterials, and biologically active molecules (Vacanti, 1993).

As tissue engineering advances, various technologies are developed, such as cell sheet engineering (Kobayashi, Kikuchi, Aoyagi, & Okano, 2019) (Imashiro & Shimizu, 2021), microfluidics (Tong & Voronov, 2022)(Weigel, Li, Fery, & Thiele, 2023), electrospinning (Hong, Yeo, Yang, & Kim, 2019)(Y. Li et al., 2021), and 3D bioprinting (Agarwal et al., 2020). Among these techniques, 3D bioprinting, a form of additive manufacturing, has become one of the leading biofabrication techniques in the pursuit of creating tissue constructs (Hospodiuk

et al., 2017)(Jain et al., 2022)(Datta et al., 2017)(Ahadian & Khademhosseini, 2018)(Chung et al., 2013)(Karamchand et al., 2023). The versatility of 3D bioprinting enables the fabrication of intricate structures with controllable architecture that are unattainable with conventional scaffolding or biofabrication techniques (Karamchand et al., 2023).

1.2 Three-dimensional (3D) bioprinting

In 3D bioprinting, a biomaterial containing cells and biomolecules, known as bioink, is deposited in a layer-by-layer fashion according to a computer-aided model (CAD) to form tissue-like constructs upon crosslinking (Unagolla & Jayasuriya, 2020), as shown in **Erreur ! Source du renvoi introuvable.**. There are four major bioprinting techniques: extrusion-based (Karamchand et al., 2023), droplet-based (Gudapati, Dey, & Ozbolat, 2016), laser-assisted (Dou et al., 2021), and vat polymerization (Ng et al., 2020). Each of these modalities has its strengths and limitations, and the choice of modality depends on the desired application (Derakhshanfar et al., 2018). Figure 1.1 schematically demonstrates the main modalities of bioprinting and their classifications.

Extrusion-based bioprinting (EBB) is the most widely used biofabrication technique (Betancourt & Chen, 2022), as it offers versatile printability for a wide range of hydrogels and applications. In EBB, a bioink is extruded through fine nozzles pneumatically or mechanically (screw or piston) (Derakhshanfar et al., 2018). The pneumatic-based systems utilize air pressure, while piston and screw-driven systems use vertical and rotational mechanical forces, respectively, to extrude the bioink through fine nozzles. EBB has the advantage of printing a wide range of viscosities ($> 6 \times 10^6$ mPa·s) (Murphy & Atala, 2014); however, the printing of high-viscosity bioinks entails high stress, which can adversely impact cell viability (Ozbolat & Hospodiuk, 2016). Other limitations of EBB include the poor printing resolution of low viscosity bioinks, complexity in fabricating hollow and free-standing constructs (Ravanbakhsh et al., 2021). Therefore, several techniques have been developed, including coaxial or core-shell (Kjar, McFarland, Mecham, Harward, & Huang, 2021) bioprinting and embedded

bioprinting (Zeng et al., 2022), to address the limitations of conventional extrusion-based bioprinting.

Compared to extrusion-based, droplet-based bioprinting (DBB) offers high-resolution printing, as it can more precisely deposit bioinks (Datta et al., 2017)(Okubo, Qureshi, Dalgarno, Goh, & Derebail, 2019)(Takagi et al., 2019). However, DBB is limited to low viscosity bioinks (< 12 mPa·s); as high viscosity bioinks cause nozzle clogging (Kang et al., 2016)(Gudapati et al., 2016)(Takagi et al., 2019). DBB encompasses inkjet (thermal and piezoelectric), micro-valve, and electrohydrodynamic (Gudapati et al., 2016)(X. Li et al., 2020). Thermal inkjet bioprinting utilizes an actuator to heat the local bioink, creating vapor bubbles that eject the bioink droplet (Cui X, Boland T, D'Lima DD, 2012). Piezoelectric inkjet bioprinting utilizes the mechanical deformation of piezoelectric sensors when a voltage is applied to eject droplets (Wijshoff, 2010). Electrohydrodynamic bioprinting utilizes high voltage electric field, resulting from electric potential difference between the printhead and the substrate, to generate droplets, rather than squeezing the ink; electric field causes mobile ions to accumulate into a conical-shape meniscus at the nozzle orifice (Taylor cone) and ejecting droplets (Park et al., 2007). Micro-valve bioprinting uses an electromagnetic valve to generate a magnetic field when a voltage pulse is applied to generate droplets (Ng, Lee, Yeong, & Win Naing, 2017).

Laser-assisted bioprinting is a nozzle-free technique based on the principles of laser-induced forward transfer (Dou et al., 2021). Laser pulses are focused on a laser-energy absorbing layer (e.g. titanium or gold) to generate a high-pressure bubble that propels bioink droplets onto a receiver plate (Dou et al., 2021). Laser-assisted bioprinting allows the printing of viscous bioinks with high resolution and speed (Dou et al., 2021); however, it is costly, and the high laser energy could result in lower cell viability compared to other bioprinting methods (Betancourt & Chen, 2022). Light-assisted/vat polymerization bioprinting is also a nozzle-free technique that utilizes a vat of photocurable bioink and ultraviolet (UV) or laser radiation to selectively crosslink the bioink and fabricate constructs (Melchels, Feijen, & Grijpma, 2010)(Ng et al., 2020), as shown Figure 1.1. However, the process is time consuming, and the use of high intensity UV could compromise the cell viability.

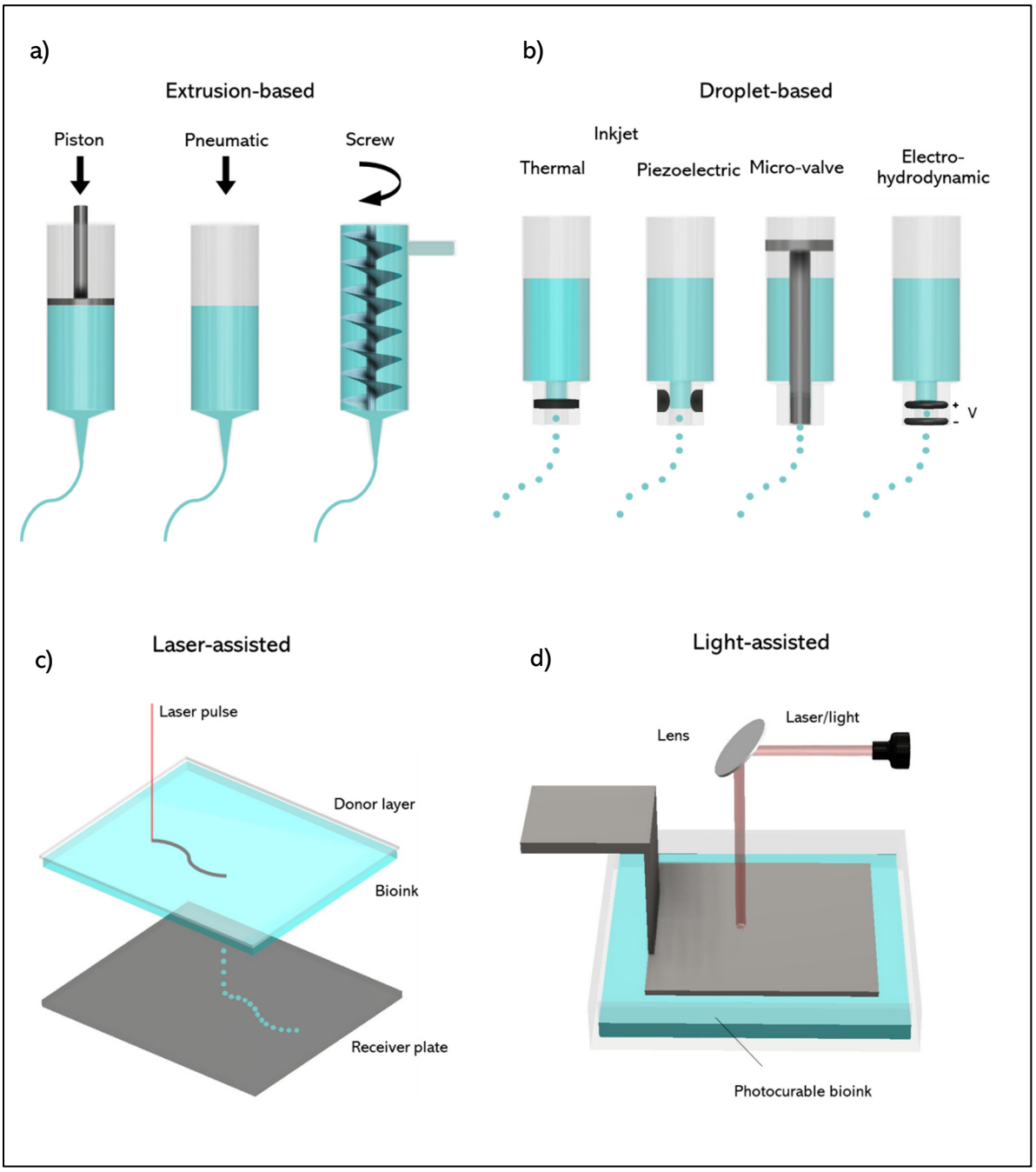

Figure 1.1 Schematic representation of 3D bioprinting modalities
a) extrusion-based compromising of pneumatic, piston-, and screw-based, b) droplet-based: inkjet (thermal, piezoelectric, micro-valve, electrohydrodynamic), c) laser-assisted, and d) vat-polymerization

1.3 Hydrogel biomaterials

Hydrogels are crosslinked polymers and are among the most common biomaterials used in bioprinting due to their biocompatibility, high-water absorbing properties, and ability to closely mimic cellular microenvironments (Drury & Mooney, 2003)(F. Xu et al., 2022). There are two main types of hydrogels: naturally and synthetically derived hydrogels. Natural polymers include collagen (extracellular matrix (ECM)) (Osidak, Kozhukhov, Osidak, & Domogatsky, 2020), gelatin (ECM) (X. Wang et al., 2017), fibrin (ECM) (de Melo et al., 2020), alginate (marine algae, seaweed, bacteria) (Augst, Kong, & Mooney, 2006), agarose (seaweed) (López-Marcial et al., 2018), and chitosan (crustaceans) (Taghizadeh et al., 2022). Natural hydrogels are inherently biocompatible, closely mimic native ECM, and mostly have natural ligands that allow cell attachment and proliferation; however, they have poor mechanical properties and fast/uncontrolled degradation (Cao, Duan, Zhang, Cao, & Zhang, 2021). On the other hand, synthetic polymers such as poly(ethylene glycol) (PEG), poly(N-isopropylacrylamide) (PNIPAM), and poly(vinyl alcohol) (PVA) possess tunable mechanical and chemical properties, but are often prepared using toxic solvents, have low cytocompatibility and must be functionalized with ECM proteins such as fibronectin or laminin, or ECM-mimetic peptides such Arg-Gly-Asp (RGD) to provide a cell friendly environment (Khoeini et al., 2021). Additionally, natural and synthetic hydrogels (hybrids) are combined in an effort to achieve the desired mechanical and biochemical properties for various applications (Ahmad et al., 2022).

Biomaterial precursors undergo a sol-gel-phase change to form hydrogels, known as crosslinking. There are various gelation methods including thermal (agarose, gelatin) (López-Marcial et al., 2018)(X. Wang et al., 2017), ionic (alginate) (Augst et al., 2006), pH (collagen) (Osidak et al., 2020), photo (GelMA) (Ying, Jiang, Yu, & Zhang, 2018), and enzymatic (fibrin) (de Melo et al., 2020) crosslinking. Thermo-repsonsive polymers such as agarose or gelatin form a hydrogel when a certain sol-gel transition temperature is reached. Photo-crosslinkable polymers, such as GelMA, solidify when exposed to visible, UV, or laser light in the presence of photo-initiators; the type of photo-initiators present in the polymer dictate the wavelength

required and crosslinking rate. Another method of crosslinking hydrogels is the use of enzymes as catalysts to promote the crosslinking/formation of covalent bonds between polymers. For instance, transglutaminase and thrombin are enzymes used to crosslink gelatin and fibrinogen, respectively. Among these, ionically crosslinking hydrogels are one of the commonly used due to their ease of crosslinking, rapid gelation kinetics, and crosslinking occurring under mild and physiological conditions (Ashammakhi et al., 2019)(F. Xu et al., 2022).

Sodium alginate is the most employed ionically crosslinking polymers in the biofabrication field (Augst et al., 2006). Alginate is a natural polymer derived from marine algae, seaweeds, or bacteria (Draget & Taylor, 2011)(K. Y. Lee & Mooney, 2012). Alginate is a linear anionic polysaccharide composed of b-D-mannuronic acid (M) and a-L-guluronic acid (G) (H. Zhang, Cheng, & Ao, 2021). Sodium alginate can form hydrogels by ionic crosslinking, known as the "egg-box" model (Grant, Morris, Rees, Smith, & Thom, 1973)(Hu, Lu, Mata, Nishinari, & Fang, 2021), as shown in Figure 1.2. Gelation occurs when di- or multi-valent ions such as Ca^{2+}, Ba^{2+}, Cu^{2+}, Sr^{2+}, Fe^{2+}, Zn^{2+}, Mn^{2+}, Al^{3+}, Fe^{3+}, react with alginate, substituting sodium ions, and binding to free carboxyl groups present in the G block (Hu et al., 2021). Among these, calcium ions (Ca^{2+}) have been the most studied/used in the literature (Ahn, Lee, Bonassar, & Kim, 2012)(Gonzalez-Fernandez, Tenorio, Campbell, Silva, & Leach, 2021). The degree of crosslinking is dictated by the alginate and crosslinker concentrations, gelation duration, and affects the mechanical properties and porosity of the structure (N. Wang, Adams, Buttery, Falcone, & Stolnik, 2009)(Jang et al., 2014). Despite sodium alginate's biocompatibility and ease of gelation, its low viscosity and rapid crosslinking can pose challenges when printed and crosslinked using conventional bioprinting methods. Therefore, to improve the printing resolution, shape fidelity, and layer adhesion of calcium alginate constructs, a variety of crosslinking strategies have been implemented (**Erreur ! Source du renvoi introuvable.**).

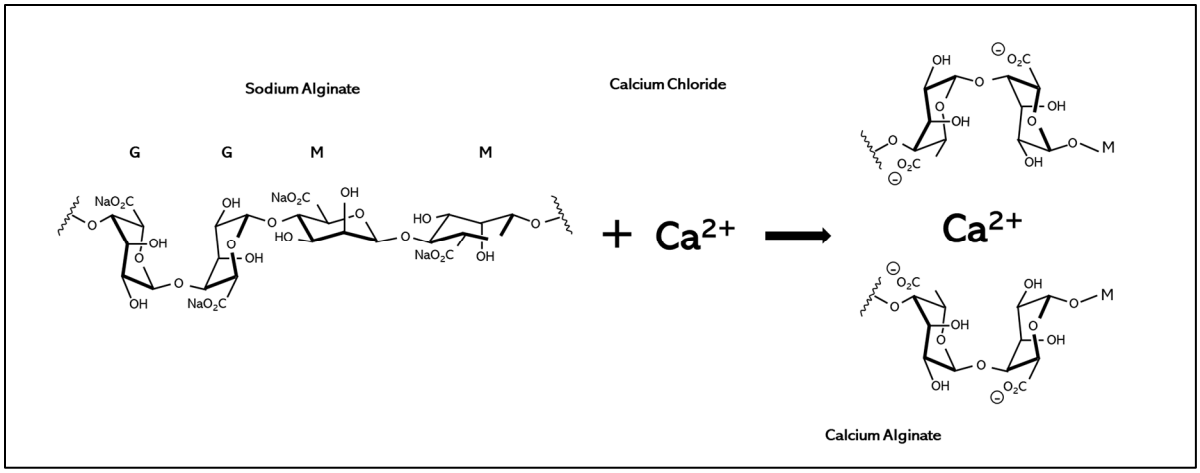

Figure 1.2 Schematic representation of ionic crosslinking of alginate with Ca^{2+} ions

1.4 Current methods of bioprinting ionically crosslinking hydrogels

Various printing and crosslinking strategies have been developed to improve the printing resolution, shape fidelity, and layer adhesion of the printed constructs (Figure 1.3). One approach to print ionically crosslinking hydrogels is partially crosslinking (low concentrations of crosslinker) the precursor bioink prior to printing and further crosslinking thereafter (Tabriz, Hermida, Leslie, & Shu, 2015)(Chung et al., 2013); however, crosslinked hydrogels cannot be easily extruded through nozzles and entails high shear stress, which can adversely impact cell viability (Ozbolat & Hospodiuk, 2016). Furthermore, partially crosslinking the precursor can cause non-uniform gelation. Additionally, droplet-based bioprinting is limited to low-viscosity bioinks, as high-viscosity bioinks cause nozzle clogging (Gudapati et al., 2016)(Takagi et al., 2019).

Another approach is submerging the printing stage in a liquid bath crosslinker while the bioink is being printed (Tabriz et al., 2015)(Christensen et al., 2015). However, printing directly in liquid crosslinking causes over-gelation, and thus, prevents good adhesion between the printed layers (Ahn et al., 2012). Moreover, a high concentration of crosslinker is detrimental to cell life (Naghieh, Karamooz-Ravari, Sarker, Karki, & Chen, 2018)(Karamchand et al., 2023).

Another printing strategy is sequentially depositing the bionk and liquid crosslinker onto the printbed (T. Xu et al., 2013)(Faulkner-Jones et al., 2015)(Sakai, Ueda, Gantumur, Taya, & Nakamura, 2018)(Sakurada, Sole-Gras, Christensen, Wallace, & Huang, 2020)(Kotlarz, Ferreira, Gentile, Russell, & Dalgarno, 2022). Although this method provides adequate crosslinking of the bioink, the printing resolution is compromised due to the bioink droplets/filament spreading upon impact onto the print stage (before gelation has occurred) (Gudapati et al., 2016).

Another developed method is printing the crosslinker coaxially along the bioink using microfluidic nozzles to improve the printability of the bioink and reduce the shear stress on cells (Zhu et al., 2018)(Colosi et al., 2014) (Kjar et al., 2021)(Restan Perez, Sharma, Masri, & Willerth, 2021). A similar approach but with an opposite configuration is utilized to create hollow tubular fibers; the bioink is extruded as the sheath flow with a crosslinker or sacrificial core (Y. Zhang, Yu, Chen, & Ozbolat, 2013)(Gao, He, Fu, Liu, & Ma, 2015). However, the excess sheath flow could also cause over-gelation and negatively impact the shape fidelity and layer adhesion of the printed structures.

To address the issues associated with excess crosslinker, further developments featuring liquid crosslinker collection mechanisms have been developed, where excess liquid is collected through an absorptive tissue or a vacuum chuck beneath the print stage (Sakurada et al., 2020). (Beyer, Bsoul, Ahmadi, & Walus, 2013). However, with these systems, the flow of liquid crosslinker during printing could still disrupt the printed structure, and the absorptive tissue may become saturated with liquid crosslinker during printing (Sakurada et al., 2020). Moreover, these methods are limited to printing on mesh-specific substrates. It can be concluded that the use of liquid crosslinker compromises the quality of the printed structures by causing poor layer adhesion due to over-gelation and poor resolution due to droplet spreading, respectively (Gudapati et al., 2016). Furthermore, the use of liquid crosslinker can cause the leaching of embedded bioactive compounds and diminish cell viability (Labay, Hamouda, Tampieri, Ginebra, & Canal, 2019)(Ng et al., 2021).

Alternative methods have been developed to address the challenges associated with liquid crosslinker, including printing in a support bath, or using sacrificial materials supplemented with the crosslinker (S. Li et al., 2023). In embedded bioprinting, a bioink is extruded within a support medium that exhibits Bingham plastic-like characteristics; a viscoelastic medium that behaves as a rigid body at low stress, but fluid-like at high shear stress (Shiwarski, Hudson, Tashman, & Feinberg, 2021). Embedded bioprinting allows the printing of low viscosity bioinks, as it maintains the shape and structure of the printed tissue constructs during and after printing until its crosslinked. Bioinks have been printed into thermoreversible hydrogels composed of gelatin microparticles (Hinton et al., 2015), Carbopol microgels (Bhattacharjee et al., 2015), or Pluronic F-127 (Liu et al., 2017). Of these, printing in gelatin microparticles, known as freeform reversible embedding of suspended hydrogels (FRSH) have gained the most attention in the field of bioprinting (Hinton et al., 2015). While these methods allow for the printing of complex and hollow structures, they require post-processing steps and longer crosslinking times; the removal of the support or sacrificial material could be challenging, time-consuming, disrupt the printed structures, and affect cell viability (Galarraga, Kwon, & Burdick, 2019).

Alternatively, the crosslinker can be introduced in mist form during or after printing (Ahn et al., 2012)(B. Zhang et al., 2017)(Yoon et al., 2018)(Raddatz et al., 2018)(G. Lee, Kim, Chun, & Park, 2021). However, the accumulation of crosslinker on the print stage (Ahn & Kim, 2015), makes the precise positioning of droplets/hydrogel and the constructs difficult and, therefore, negatively impacts the shape fidelity of the printed constructs. Therefore, an improved system is required to control the crosslinking rate to ensure good shape fidelity and layer adhesion. Additionally, an improved collection mechanism must be developed to prevent the accumulation of crosslinker on the print stage.

MacCallum et al., has recently developed a novel mist-based system for extrusion-based bioprinting that enables the fabrication of 3D ionically crosslinking hydrogel construct with excellent shape fidelity and strong layer adhesion (MacCallum et al., 2020). The crosslinker is generated and delivered into a printhead attachment to crosslink a flowing hydrogel stream and

features a mist removal mechanism to prevent the accumulation of crosslinker on the printbed (MacCallum et al., 2020). However, mist-based technology has not yet been applied to droplet-based and coaxial bioprinting, which could help address the limitations associated with these modalities.

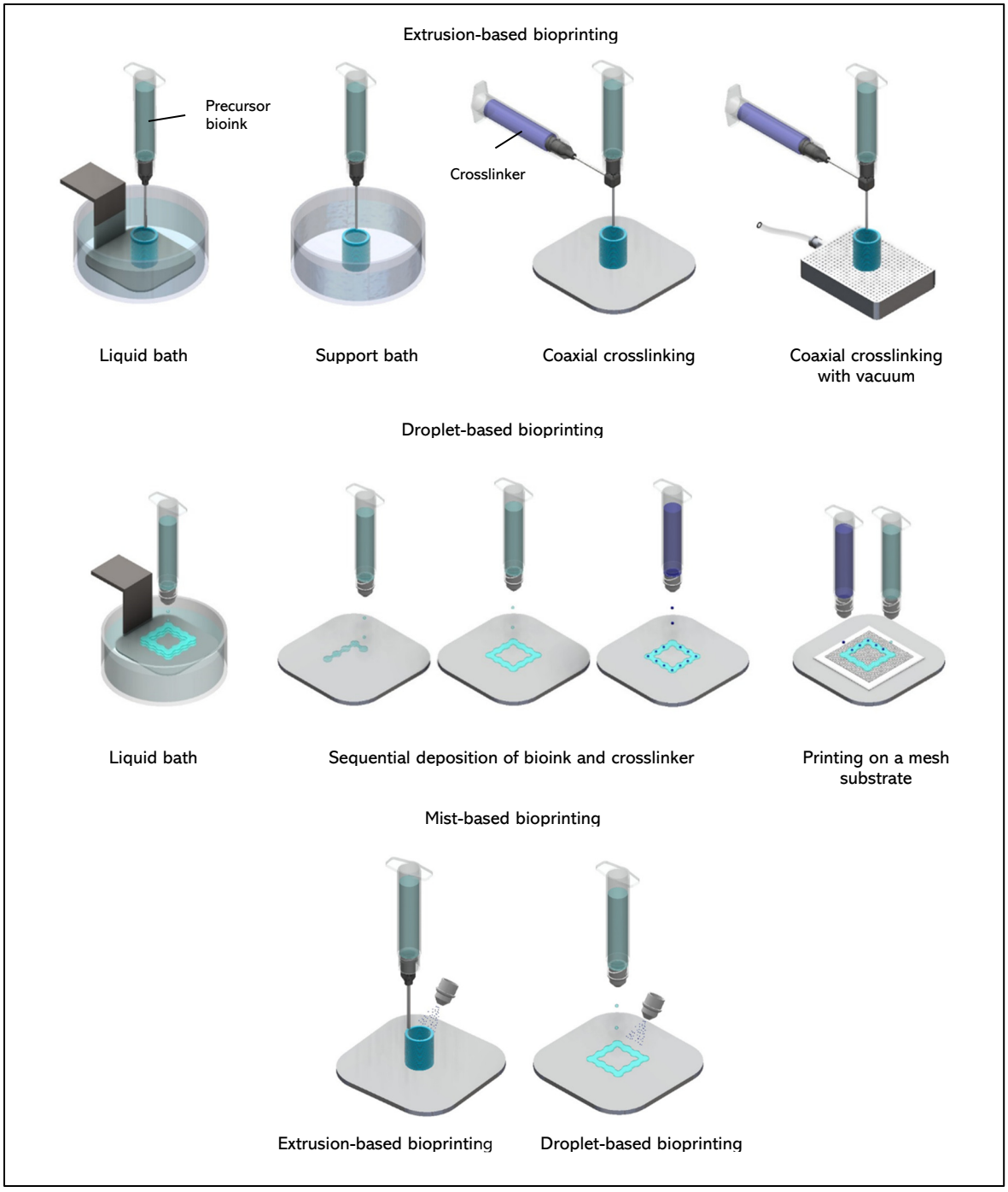

Figure 1.3 Bioprinting strategies of ionically crosslinking hydrogels

Table 1.1 Crosslinking strategies

Bioprinting modality	Crosslinking technique	Description	Advantages	Limitations	Refs.
Extrusion-based	Partial crosslinking	- Pre-mixing the precursor and crosslinker.	- Optimized printing viscosity for printing.	- Non-uniform crosslinking. - High shear stress that impacts cell viability. - Limited to extrusion-based bioprinting.	(Tabriz et al., 2015)(Chung et al., 2013)
	Liquid bath	- Deposition of precursor into crosslinker bath.	- Provides adequate crosslinking.	- Poor layer adhesion.	(Tabriz et al., 2015)(Piras & Smith, 2020)
	Embedded bioprinting	- Printing of precursor within a support bath supplemented with crosslinker.	- Allows bioprinting of low viscosity bioinks. - Can create complex and hollow structures.	- Requires post-processing steps. - Longer crosslinking times. - Limited to extrusion-based bioprinting.	(Hinton et al., 2015)
	Coaxial crosslinking	- Inline crosslinking.	- Improved crosslinking resolution.	- Accumulation of crosslinker on printbed.	(Colosi et al., 2016) (Gao et al., 2015)
	Removal	- Removes excess crosslinker using a vacuum chuck.	- Prevents accumulation of crosslinker on printbed.	- Limited to printing on specific substrates - Causes distortion to the printed structure.	(Beyer et al., 2013)
	Mist	- Introducing the crosslinker in mist form.	- Controlled gelation.	- Accumulation of crosslinker on printbed.	(Raddatz et al., 2018)(Ahn et al., 2012)
Droplet-based	Liquid bath	- Deposition of bioink into crosslinker bath.	- Provides adequate crosslinking.	- Droplet spreading. - Poor layer adhesion.	(Christensen et al., 2015)
	Alternate layers	- Deposition of precursor and crosslinker sequentially.	- Provides adequate crosslinking.	- Bioink droplet spreading and splashing on the printing substrate. - Accumulation of crosslinker on printbed.	(T. Xu et al., 2013)
	Removal	- Printing on a mesh substrate.	- Collects excess crosslinker.	- Saturation of absorptive tissue with liquid crosslinker - Limited to printing on a specific substrate.	(Sakurada et al., 2020)
	Mist	- Introducing crosslinker in mist form.	- Controlled gelation	- Accumulation of crosslinker on printbed.	(Yoon et al., 2018)

1.5 Research objectives

The aim of this thesis is to investigate the suitability of mist-based crosslinking for droplet-based and coaxial crosslinking of ionically crosslinking hydrogels. The objectives of this thesis are defined as follows:

Objective 1: develop a mist-based printhead for droplet-based bioprinting of ionically crosslinking hydrogel bioinks. ii. characterize the impact of printing parameters on printability, shape fidelity, and the mechanical properties. iii. assess the biocompatibility of the printing structures.

Objective 2: i. develop a mist-based technique that allows bioprinting of hollow fibers. ii. characterize the impact of printing parameters on the diameter, wall thickness, and the mechanical properties of the hollow filaments. iii. assess the biocompatibility of the printing structures.

CHAPTER 2

MATERIALS AND METHODS

2.1 Theory

2.1.1 Diffusion calculation for bioink droplets

The diffusion of crosslinker ions and, hence, controlled gelation of the bioink droplets is important for co-droplet adhesion (Figure 2.1(a)). The diffusion of crosslinker ions (Ca^{2+} in this study) into printed droplets is assumed to obey Fick's second law of diffusion. The one-dimensional, radial diffusion equation of the crosslinker ions into a droplet can be defined as (Djelveh, Gros, & Bories, 1989)

$$\frac{\partial C}{\partial t} = D_c \left(\frac{\partial^2 C}{\partial r^2} + \frac{2}{r}\frac{Cr}{\partial r}\right), \tag{2.1}$$

where D_c is the diffusion coefficient of crosslinker ions (m^2/s) within the droplet medium, C is the concentration of the crosslinker ions, r is the radial distance (m), and t is time (s).
The concentration, C, of crosslinker ions within the droplet at radial distance, r, and time, t, is calculated as (Westwater & Drickamer, 1975)

$$C = C_s + C_s \left(\frac{2a}{\pi r}\sum_{n=1}^{\infty}\frac{(-1)^n}{n} sin\left(\frac{n\pi r}{a}\right) e^{-\left(\frac{D_c n^2 \pi^2 t}{a^2}\right)}\right), \tag{2.2}$$

where C_s is the crosslinker concentration at the surface of the droplet and a is the radius of the droplet (m) (Figure 2.1(b)). The concentration at the center of the droplet, C_c, is determined by restating equation (2.2) where r approaches zero, as

$$C_c = C_s + 2C_s \sum_{n=1}^{\infty}(-1)^n e^{-\left(\frac{D_c n^2 \pi^2 t}{a^2}\right)}. \tag{2.3}$$

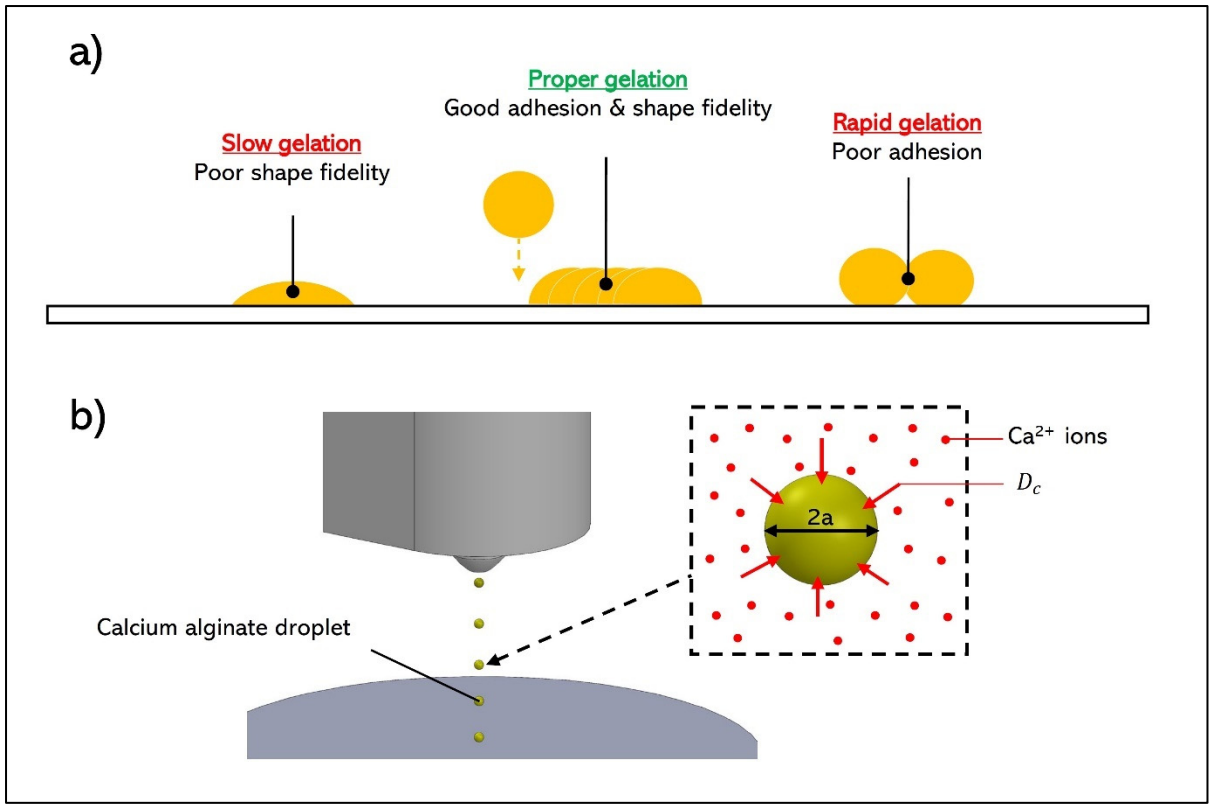

Figure 2.1 Diffusion of crosslinker into printed droplet
a) effects of droplet gelation on shape fidelity and co-droplet adhesion. b) Model demonstration diffusion of Ca^{2+} ions into the printed droplet. Reprinted with permission(Badr et al., 2022)

The depth of penetration is calculated to be smaller than 4% of the radius which confirms the partial crosslinking of the printed droplets (Figure 2.2). Although the droplet internal flow plays an important role in circulation of penetrated calcium ions and re-distributing them within the droplet, the crosslinking remains partial due to the small amounts of penetrated ions.

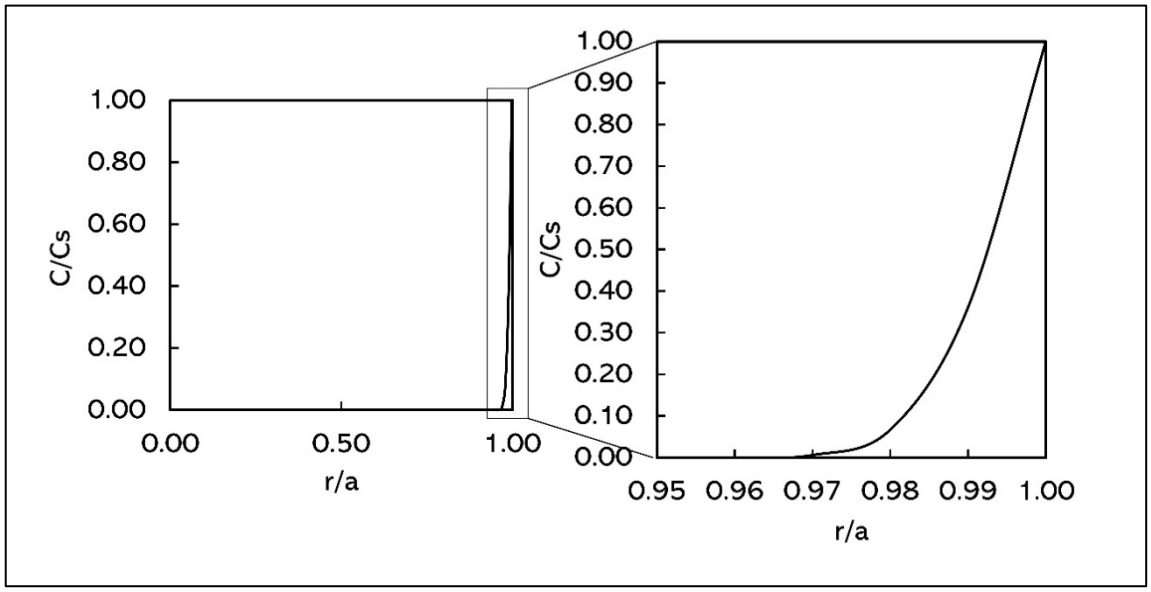

Figure 2.2 Theoretical Concentration distribution of Ca^{2+} within a droplet at the time of impact. (Badr et al., 2022)

2.2 Material preparation

Sodium alginate solutions (1, 2, 3, and 4 wt%) are prepared by dissolving sodium alginate powder (Sigma-Aldrich, USA) in deionized (DI) water and stirred at 500 rpm for 2 hours. Calcium chloride ($CaCl_2$) solutions (1, 5, 10, and 20 wt%) are prepared by dissolving calcium chloride powder (Sigma-Aldrich, USA) in DI at 200 rpm for 30 min. Solutions are stored at room temperature.

2.3 Mist-based printhead attachment

The misting printhead attachment is designed using 3D CAD software (Solidworks, Dassault Systems) and fabricated with photopolymer resin using selective laser sintering (SLS) 3D printing (Form3, FormLabs). The misting printhead attachment fits to the droplet/pneumatic printhead of a 3D bioprinter and facilitates the transport of crosslinker mist; mist is delivered via an inlet port and then collected via an outlet port. Bioink droplets/filaments pass through the continuous flow of mist within the central channel, enabling crosslinking before deposition onto the print stage.

2.4 3D bioprinting setup

2.4.1 Droplet-based

The printhead attachment is fitted to a microvalve-based droplet printhead onboard a commercial 3D bioprinter (BioX, Cellink), as shown in Figure 2.3(b); based on the flow simulation results (Figure AI.1), the diameter of printhead channel is chosen to be 4 mm. The 3D bioprinter commands *x*-, *y*- and *z*-axis motion and droplet ejection characteristics; printing speed is set at 5 mm/s, and valve open and delay times are set to 1 and 100 ms, respectively. Sodium alginate solution in a 3 mL syringe is loaded into the droplet printhead and connected to a pneumatic supply. The syringe pressure is not reported to have a significant effect on the droplet diameter for microvalve systems (Ng et al., 2017); however, the pressure is adjusted specifically for each bioink solution to prevent nozzle clogging or splashing upon impact with the print stage. Mist is generated using an ultrasonic atomizer (B00P8OYGNA, AGPtek) submersed in $CaCl_2$ in a 500 mL polypropylene jar. An air pump ($\leq$1500 mL/min) drives the flow of mist into the printhead attachment inlet, and a vacuum pump ($\leq$5 L/min) collects the mist at the outlet, as shown in Figure 2.3(c).

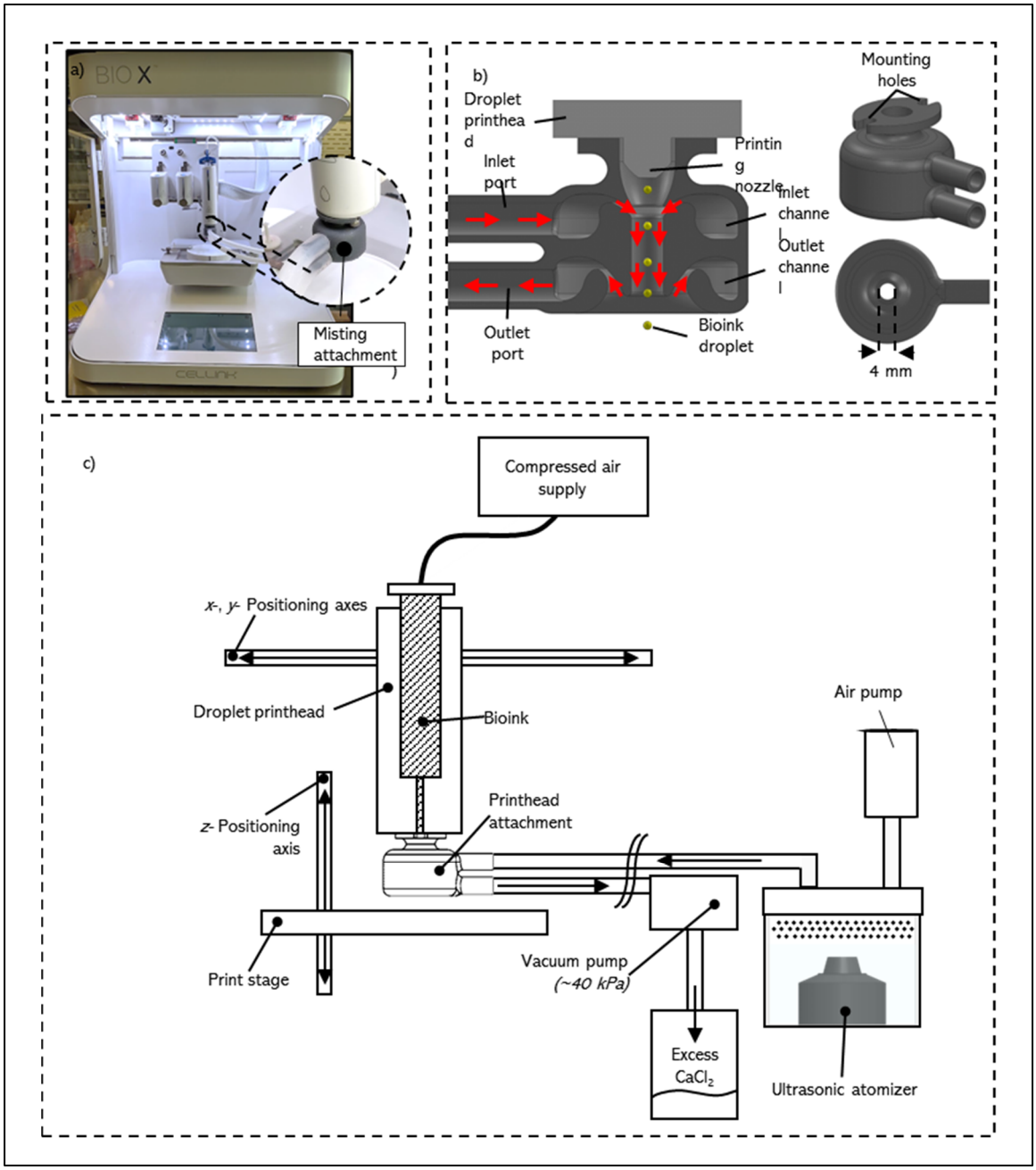

Figure 2.3 3D printing set-up for DBB
a) Printing setup using droplet-based printhead attachment on Bio X 3D bioprinter. b) CAD model of mist-based printing head attachment for DBB. c) System-level diagram of printing setup using misting printhead attachment. Reprinted with permission (Badr et al., 2022)

2.4.2 Coaxial set-up

A mist-based coaxial 3D printing system is used to fabricate hollow fibers, as shown in Figure 2.4. A coaxial nozzle (Allevi, 3D SYSTEMS) composed of a 20-gauge inner needle (584 μm inner diameter (ID), 889 μm outer diameter (OD)) and 16-gauge outer needle (1190 μm ID, 1650 μm OD), is fitted to a pneumatic-based printhead onto a commercial 3D bioprinter (Bio X, Cellink). Sodium alginate solution (2, 3 and 4 wt%) in 5 mL syringe is loaded on a syringe pump (Fusion 100, Chemyx). Hollow fibers and multi-layer hollow fiber scaffolds are fabricated by delivering $CaCl_2$ mist/sodium alginate solution through the core/shell nozzle. To generate and deliver atomized $CaCl_2$, a mist-based system is used, as previously described (Badr et al., 2022). Briefly, an ultrasonic atomizer (B00P8OYGNA, AGPtek), submerged in a $CaCl_2$ solution, is used to generate $CaCl_2$ mist droplets. Mist is pneumatically forced using an air pump into the printhead to crosslink the hollow fiber during printing. Unless otherwise stated, the printing speed, mist core pressure, and sodium alginate flowrate are set to 25 mm/s, 5 kPa, and 15 mL/hr, respectively.

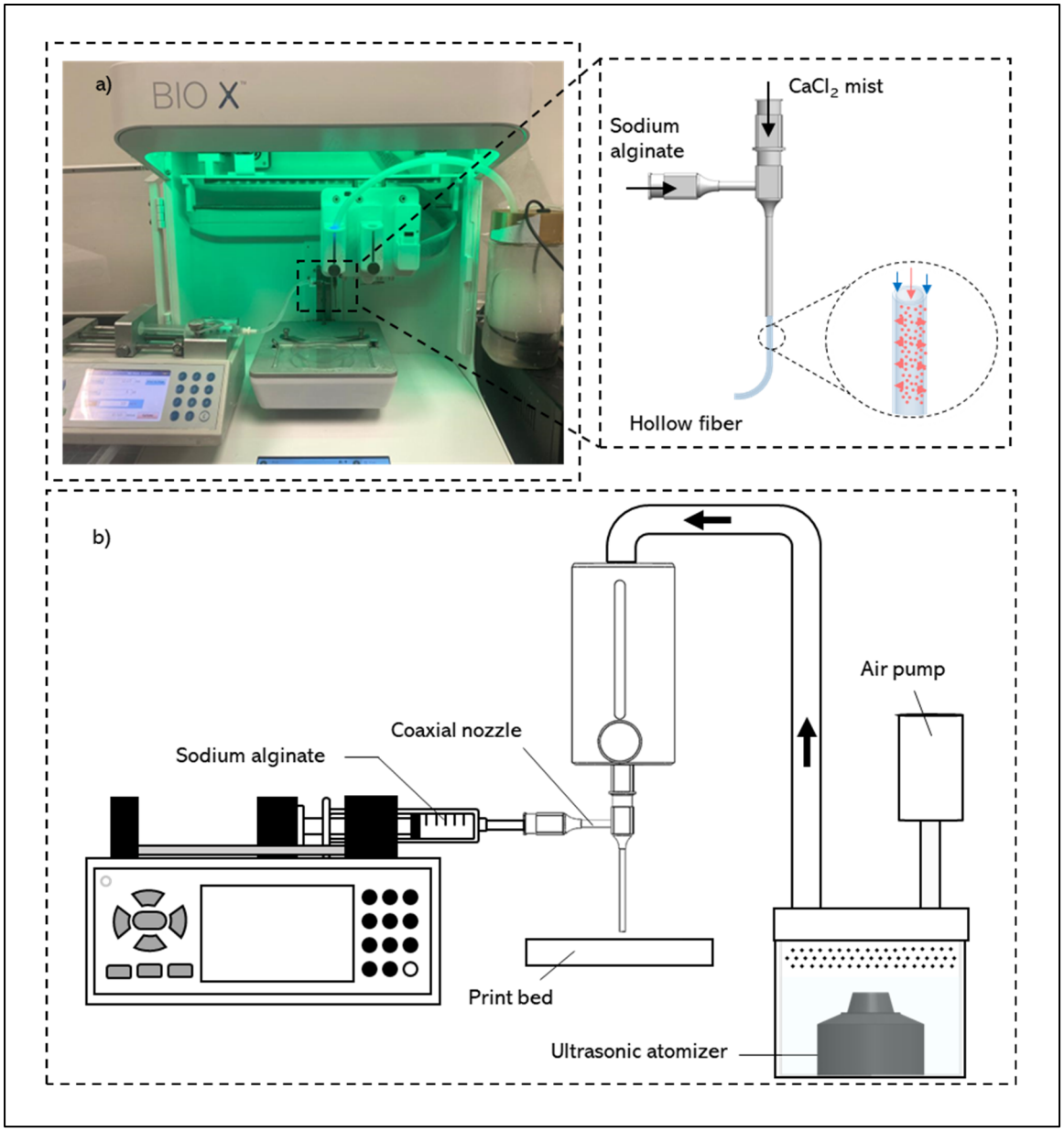

Figure 2.4 3D mist-based coaxial bioprinting setup
a) Printing setup of a coaxial nozzle mounted onto a 3D bioprinter showing the mist-based crosslinking method. b) System-level diagram of coaxial extrusion bioprinting and mist generation setup

2.5 Droplet impact characterization

The effects of the crosslinking mechanism on the spreading factor of 2 wt% sodium alginate droplets on a hydrophobic surface (contact angle = 95°) is investigated. The droplets are ejected 27 mm away from the printbed. The spreading factor of the droplet is calculated as (Werner, Jones, Paterson, Archer, & Pearce, 2007)

$$\text{Spreading factor} = \frac{D(t)}{D_{\text{i}}}, \tag{2.4}$$

where $D(t)$ is the diameter of the droplet contact area at time, t, and D_{i} is the initial droplet diameter at the time of printing. The set-up used to image the droplet impact on the print stage is shown in Figure 2.5. A high-speed camera (FASTCAM SA-X2, HSI) at a speed of 40,000 fps is utilized to capture the droplet impact, a light source (LED-BL, PHLOX) is used to enhance the contrast, and image analysis (ImageJ, NIH) is used to measure the initial droplet diameter, transient diameter, and impact velocity. The spreading factor is measured with no mist, and with 10 wt% and 40 wt% $CaCl_2$ solutions. Additionally, the spreading factor is analyzed for two impact velocities, 2.64 m/s and 4.80 m/s.

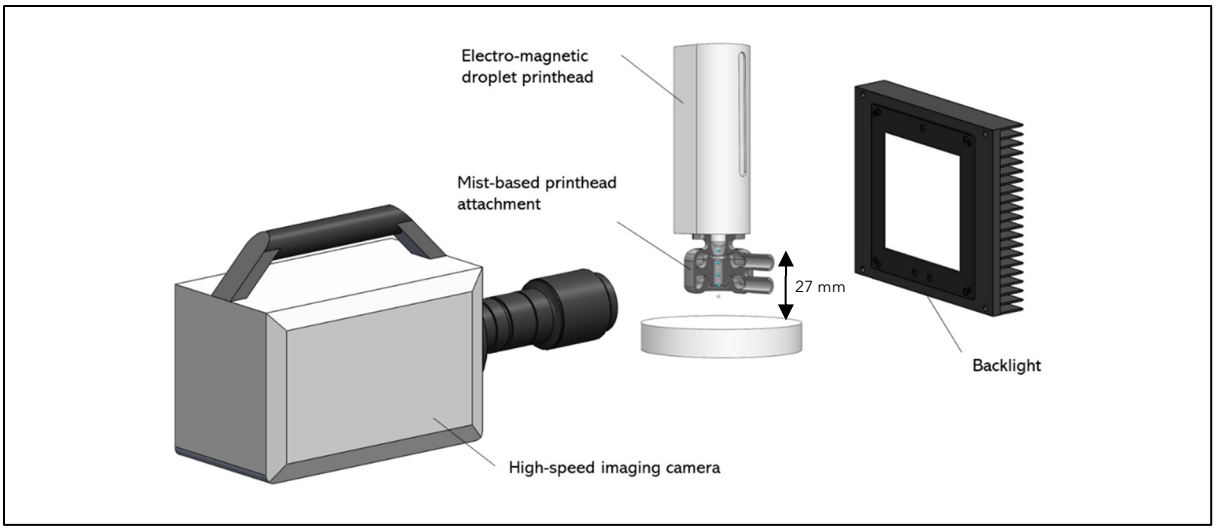

Figure 2.5 High-speed imaging of the bioink droplet impact setup

2.6 Printability analysis

The printability of scaffolds fabricated using droplet-based and coaxial systems is evaluated. The printability number, Pr, of scaffolds printed and crosslinked with different sodium alginate, mist concentrations, and flowrates is calculated Pr is defined as (Ouyang, Yao, Zhao, & Sun, 2016):

$$Pr = \frac{L^2}{16A}, \tag{2.5}$$

where L and A are the perimeter and area of the scaffold pore, respectively. A Pr value of 1 indicates ideal printability, while Pr < 1 and Pr > 1 indicate under- and over-gelation, respectively. To calculate the Pr number of the printed scaffolds, images of 2-layer, 30 × 30 mm, square scaffolds taken immediately after printing were analyzed; the perimeter and area of the pores were measured using an image processing software (Fiji, ImageJ).

2.7 Hollow fiber dimensions

The effect of the core pressure and sheath flowrate on the diameter and wall thickness of the hollow fibers are analyzed. The printed hollow fibers are visualized/imaged using a compound, brightfield microscope (T390B, AmScope) equipped with a digital camera (MU1803-HS, AmScope), and the diameter and wall thickness measurements are performed using an image processing software (Fiji, ImageJ), as shown in Figure 4.2(a). The pixel size is 0.5 μm.

2.8 Mechanical and rheological characterization

2.8.1 Rheology

A rotational rheometer (Kinexus Ultra+, Netzsch) equipped with an 8 mm plate and 1 mm tool gap is used to determine the rheological properties of sodium alginate with different

concentrations (1, 2, 3 wt%). Tests are conducted at 37 °C within a shear rate of 0.1-1000 s^{-1} at a constant frequency of 1 Hz.

2.8.2 Compression tests

Compression tests are conducted on 3-layer, 10 mm square scaffolds printed at room temperature using a rotational rheometer (Kinexus Ultra+, Netzsch) with 8 mm flat plate geometry; the modulus of elasticity is calculated within a force range of 0.3–10 N.

2.8.3 Strain tests

The mechanical properties of the hollow fibers are evaluated by measuring the breaking strain. Strain tests were conducted on 100 mm-long hollow fibers printed and crosslinked using various sodium alginate (2, 3, and 4 wt%) and mist (5, 10, 20 wt%) concentrations, respectively. The strain was calculated as (Girón-Hernández, Gentile, & Benlloch-Tinoco, 2021)

$$\varepsilon = \frac{L_{\mathrm{i}} - L_{\mathrm{f}}}{L_{\mathrm{i}}}. \tag{2.6}$$

where L_{i} and L_{f} are the initial and final lengths of the hollow fibers, respectively.

2.9 Swelling

For the droplet-based study, 2-layer, 20 mm square scaffolds were soaked in PBS at 37 °C. At different time intervals, the scaffolds were taken out, placed on filter paper to remove excess PBS, and weighted. The swollen scaffolds are then dried at 37 °C for 24 hours and weighted afterwards. The swelling ratio was calculated as (Sharma, Dinda, Potdar, Chou, & Mishra, 2016):

$$\mathrm{SR}\ (\%) = \frac{W_{\mathrm{s}} - W_{\mathrm{d}}}{W_{\mathrm{d}}} \times 100\%, \tag{2.7}$$

where Ws is the weight of the scaffold after swelling, and Wd is the weight of the scaffold dried scaffold (Sharma et al., 2016). The measurement continued until no further change in the swelling ratio is observed (9 hours).

2.10 Biocompatibility

Neuron cells (Neuro2a) are used to study the biocompatibility of the printed constructs for both the droplet-based and coaxial bioprinting studies.

2.10.1 Cell culture

Neuron cells (Neuro2a) are used to study the biocompatibility of the printed constructs. Cells are grown in culture Minimum Essential Medium (MEM) (Gibco, 11095080) supplemented with 10% Fetal Bovine Serum (Cytiva, SH3039603HI) and 2% Penicillin-Streptomycin (Gibco, 15140122) at 37 ºC in a 5% CO_2 incubator. Cells are seeded at a density of approximately 2×10^5 cells/mL in culture media. The media is changed 24 h post seeding, and then every 3 days thereafter. Cells are passaged using trypsin (0.25%) when approximately 80% confluency is reached.

2.10.2 Cell viability

The viability of Neuro2a cells seeded on scaffolds printed using 3 wt% sodium alginate and crosslinked with 10% mist and 100 mM liquid bath was evaluated over 7 days. 2-layer, 20 × 20 mm square scaffolds were printed on 35 mm culture-treated dishes, sterilized with UV light for 10 min, and seeded with approximately 300,000 Neuro-2a cells and 2 mL of culture media. As a control, cells were seeded on a petri dish without adding printed constructs. Cells were grown at 37 ◦C in a 5% CO_2 incubator, and the culture media was replaced every 3 days. Similar methods are conducted for the droplet-based study; however, neuron cells were seeded on scaffolds printed using various concentrations of alginate (1, 2, 3 wt%).

Brightfield and fluorescence imaging were performed using a Revolve 3 microscope (Echo, USA) on days 3 and 7. Neuro2a cells were stained using 4'6-diamidino-2-phenylindole dihydrochloride (DAPI) and propidium iodide (PI) at concentrations of 5 µg/mL and incubated for 15 and 30 min, respectively. Thereafter, fluorescent images of cells were acquired and analyzed using Fiji image processing software (ImageJ). Briefly, the blue (total cells) and red (damaged cells) channels and intensities were separated and normalized using a grayscale filter, respectively. The cell viability percentage was calculated as:

$$Cell\ viability\ \% = \left(1 - \frac{red\ intensity\ (damaged\ cells)}{blue\ intensity\ (total\ cells)}\right) \times 100. \qquad (2.8)$$

2.11 Statistical analysis

All experiments were performed in triplicates and data are presented as mean $\pm$ standard deviation. Statistical analyses were performed using two-way analysis of variance (ANOVA) followed by post hoc Tukey's multiple comparison test. p - value < 0.05 (*) was considered significantly different.

CHAPTER 3

DEVELOPMENT OF A MIST-BASED PRINTHEAD FOR DROPLET-BASED BIOPRINTING OF IONICALLY CROSSLINKING HYDROGEL BIOINKS

This chapter includes the results obtained for the development of a mist-based printhead for droplet-based bioprining study. The rheological properties of the hydrogel precursor are studied. The printability, mechanical properties, swelling behavior and cell viability are assessed. Results presented and discussed in this chapter are published in *Bioprinting* (Badr et al., 2022).

3.1 Rheological properties

The apparent viscosities of each concentration of sodium alginate solution are shown Figure 3.1. The viscosities of 1, 2, and 3 wt% solutions are constant within the shear rate range shown (0.1 – 1000 s^{-1}), indicating that each solution is a Newtonian liquid. The apparent viscosities of the 1, 2, and 3 wt% solutions are 9.7, 41.3, and 63.3 mPa·s, respectively.

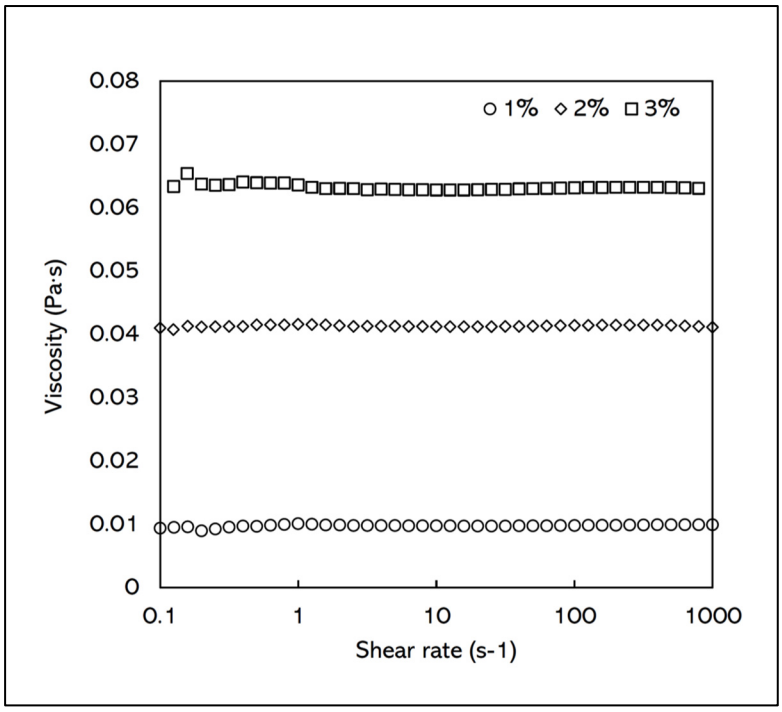

Figure 3.1 Viscosity vs. shear strain for 1, 2, 3 wt% sodium alginates

3.2 Spread factor analysis

The spreading factor graphs of 2 wt% alginate droplets with different crosslinker concentrations and impact velocities, are shown in Figure 3.2(a) and Figure 3.2(b), respectively. It is observed that the exposure of the droplet to crosslinker mist decreases the spreading factor due to crosslinking of hydrogel and the consequent increase in the viscosity (Lin et al., 2018). This is further confirmed as the use of 40 wt% $CaCl_2$ mist solution leads to a 12% decrease in spreading factor as compared to using 10 wt% mist solutions (Figure 3.2(a)). Furthermore, it is observed that the velocity of the droplet impacting the printbed has a significant effect on the spreading factor; increasing the impact speed of droplets crosslinked using 40 wt% mist from 2.64 m/s to 4.80 m/s caused a 45% increase in the spreading factor ((Figure 3.2(b)). Impacting the surface with a higher velocity results in higher spreading and higher shear stress which negatively affects the printing resolution and cell viability,

respectively (Lin et al., 2018)(Ng et al., 2021). Therefore, printing at lower impact velocities is recommended. The optimized droplet velocity for this study is determined to be 2.64 m/s.

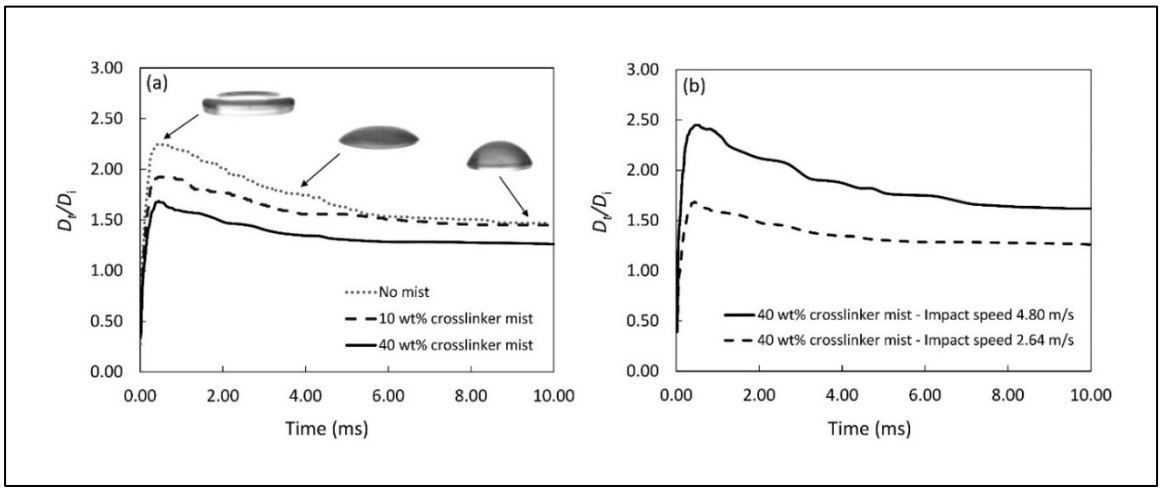

Figure 3.2 Spread factor over time
a) Spread factor without mist, with 10 wt% $CaCl_2$ mist and 40 wt% $CaCl_2$ mist. b) Spread factor at two impact velocities with 40 wt% $CaCl_2$ mist. Reprinted with permission (Badr et al., 2022)

Using mist to control the droplet spreading offers several advantages over other methods of controlling droplet spreading. For instance, as compared to controlling the droplet spreading using upward ejection (Ji et al., 2019), the use of crosslinker provides another degree of control over the dynamics of droplet spreading. Introducing crosslinker in mist form offers an advantage over the liquid crosslinkers: when crosslinker mist is used, the droplet spreading can be changed according to the interfacial properties of the printbed. Moreover, liquid crosslinkers (Haldar & Chakraborty, 2019) are not suitable for certain applications, including drug delivery constructs, as the active compounds can leach into the liquid crosslinker. Finally, as compared to the thermal crosslinking mechanisms (Jalaal, Seyfert, Stoeber, & Balmforth, 2018), the use of mist provides an enhanced degree of control over spreading of the droplets in multi-layer constructs.

3.3 Printability analysis

Scaffolds are printed to demonstrate the effects of the mist inlet flowrate on the quality of printed constructs. As shown in Figure 3.3(a), a mist flowrate of 750 mL/min results in a lack of crosslinking, as indicated by the alginate remaining as a liquid on the print stage. The optimal mist flowrate is determined to be 1250 mL/min, as demonstrated by Figure 3.3(b), wherein the printed scaffold exhibits good shape fidelity and, furthermore, strong co-droplet adhesion. This supports the findings from the flow simulation results in Figure AI.1(a). Figure 3.3(b) shows the effects of increasing the mist flowrate further to 1500 mL/min: the printed droplets are crosslinked too rapidly, resulting in poor co-droplet adhesion. Therefore, the mist flowrate must be optimized to achieve controlled gelation during deposition so that printed constructs exhibit strong co-droplet and co-layer adhesion. The multi-layer constructs shown in Figure 3.4, printed using 3 wt% sodium alginate, further demonstrate the ability of the system to print 3D geometries. The printed constructs exhibit strong layer adhesion.

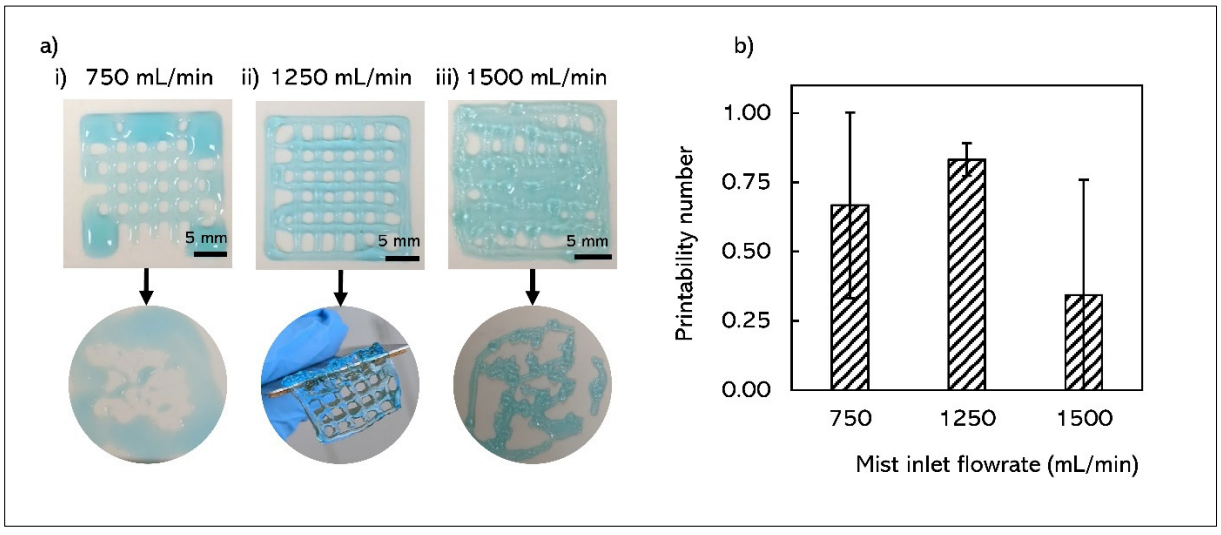

Figure 3.3 Printability analysis of scaffolds
a-i) 20 mm square scaffold printed using 3 wt% sodium alginate and a mist flowrate of 750 mL/min, exhibiting under-gelation. a-ii) Scaffold printed using 3 wt% sodium alginate and a mist flowrate of 1250 mL/min, exhibiting good gelation and shape fidelity. a-iii) Scaffold printed with 3 wt% sodium alginate and a mist flowrate of 1500 mL/min, exhibiting over-gelation and poor co-droplet adhesion. b) Printability number of scaffolds printed with 3 wt% sodium alginate droplets with diameter of ~700 µm and printbed speed of 5 mm/s crosslinked with 750, 1250, and 1500 ml/min mist flowrates.

Figure 3.4 Various geometries printed using 3 wt% sodium alginate a) top and, b) side views of 4-layer UPEI letters, c) a 2-layer scaffold, and d) 3-layer cube. Reprinted with permission (Badr et al., 2022)

3.4 Mechanical characterization

Measuring the mechanical properties of printed scaffolds reflects the extent of gelation. Square scaffolds, shown in Figure 3.4(d), are printed and the compressive modulus of each is measured. The effect of the mist inlet flowrate on the crosslinking rate is demonstrated in Figure 3.5. As shown in Figure 3.5, the lowest flowrate of 1000 mL/min produces a compressive modulus of 17.80 kPa, whereas the highest flowrate of 1500 mL/min results in a compressive modulus of 25.90 kPa. This result indicates greater gelation when increasing the mist inlet flowrate, as previously exhibited in Figure AI.1(a) and Figure 3.3.

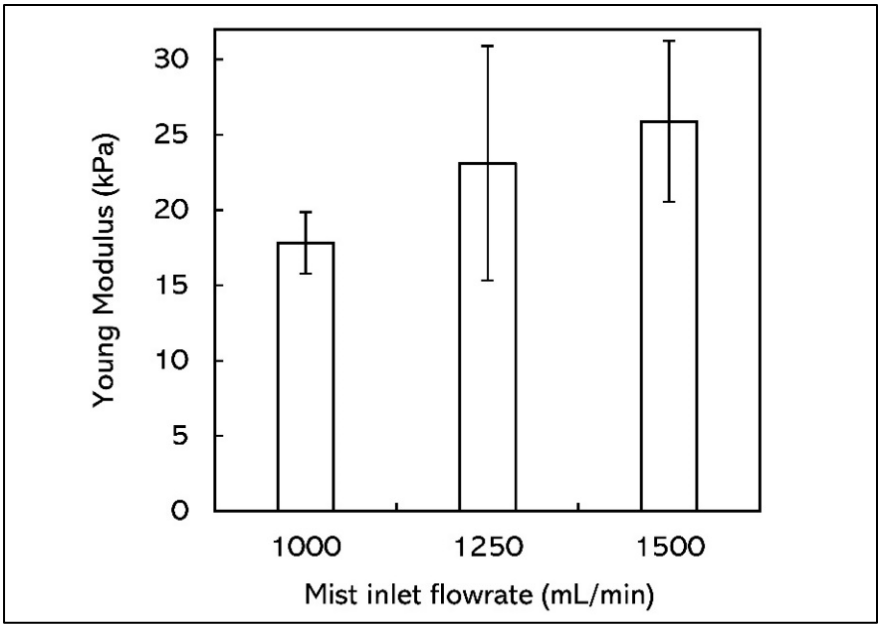

Figure 3.5 Young Modulus of scaffolds printed using 3 wt% sodium alginate with varying inlet mist flowrates. Reprinted with permission (Badr et al., 2022)

3.5 Swelling behavior

The swelling ratio of the 20 mm square scaffolds, printed using 3 wt% sodium alginate and crosslinked with different mist delivery rates, are presented in Figure 3.6. The swelling ratios of scaffolds crosslinked with mist inlet flowrates of 1000, 1250, and 1500 mL/min are 1003%,

1101%, and 1100%, respectively. These results are comparable to previous studies (Yang et al., 2018). The scaffold crosslinked with a mist inlet flowrate of 1000 mL/min shows the lowest swelling ratio; however, statistical analysis suggests no significant difference between all samples ($p > 0.05$).

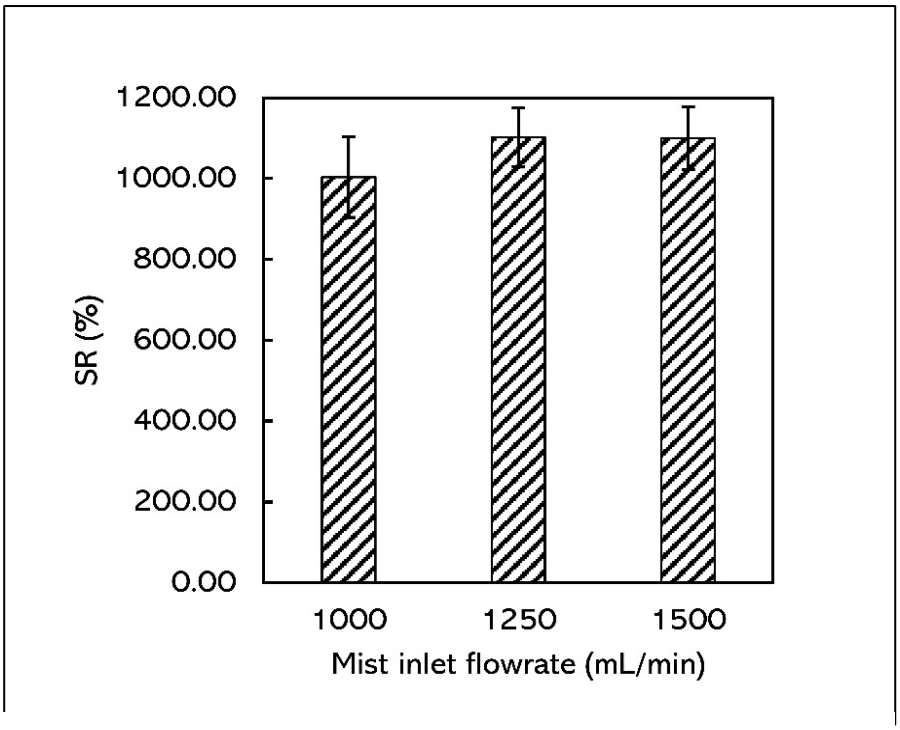

Figure 3.6 The swelling ratios (after 9 hour) of scaffolds printed with 3 wt% sodium alginate droplets with diameter of ~700 μm and printbed speed of 5 mm/s crosslinked with 1000, 1250, and 1500 mist inlet flowrates. Reprinted with permission (Badr et al., 2022)

3.6 Biocompatibility

2-layer, 20 mm square constructs are printed with three concentrations of sodium alginate, 1 wt%, 2 wt%, and 3 wt%. Cell viability is monitored over 4 days with fluorescence imaging performed on days 3 and 4. Seeded cells on the printed constructs show growth over the culturing period, as shown in Figure 3.7 and Figure 3.8. As shown in Figure 3.8, the seeded cells show a high level of viability. As shown in Figure 3.8, the average viability values on

day 3 for control and concentrations 1 wt%, 2 wt%, and 3 wt% are 97%, 98%, 99%, and 99%, respectively. The average viability values on day 4 for control and concentrations 1 wt%, 2 wt%, and 3 wt% are 89%, 99%, 98%, and 92%, respectively. The viability values are smaller on day 4 as compared to day 3 and the 1 wt% sodium alginate bioink shows the highest viability values. The decrease in cell viability is due to confluency (Butler, Naseri, MacDonald, Andrew Tasker, & Ahmadi, 2020). Overall, the results show that the printed constructs are biocompatible, and that there is no significance difference between the cell viability at different concentrations of sodium alginate on the same day.

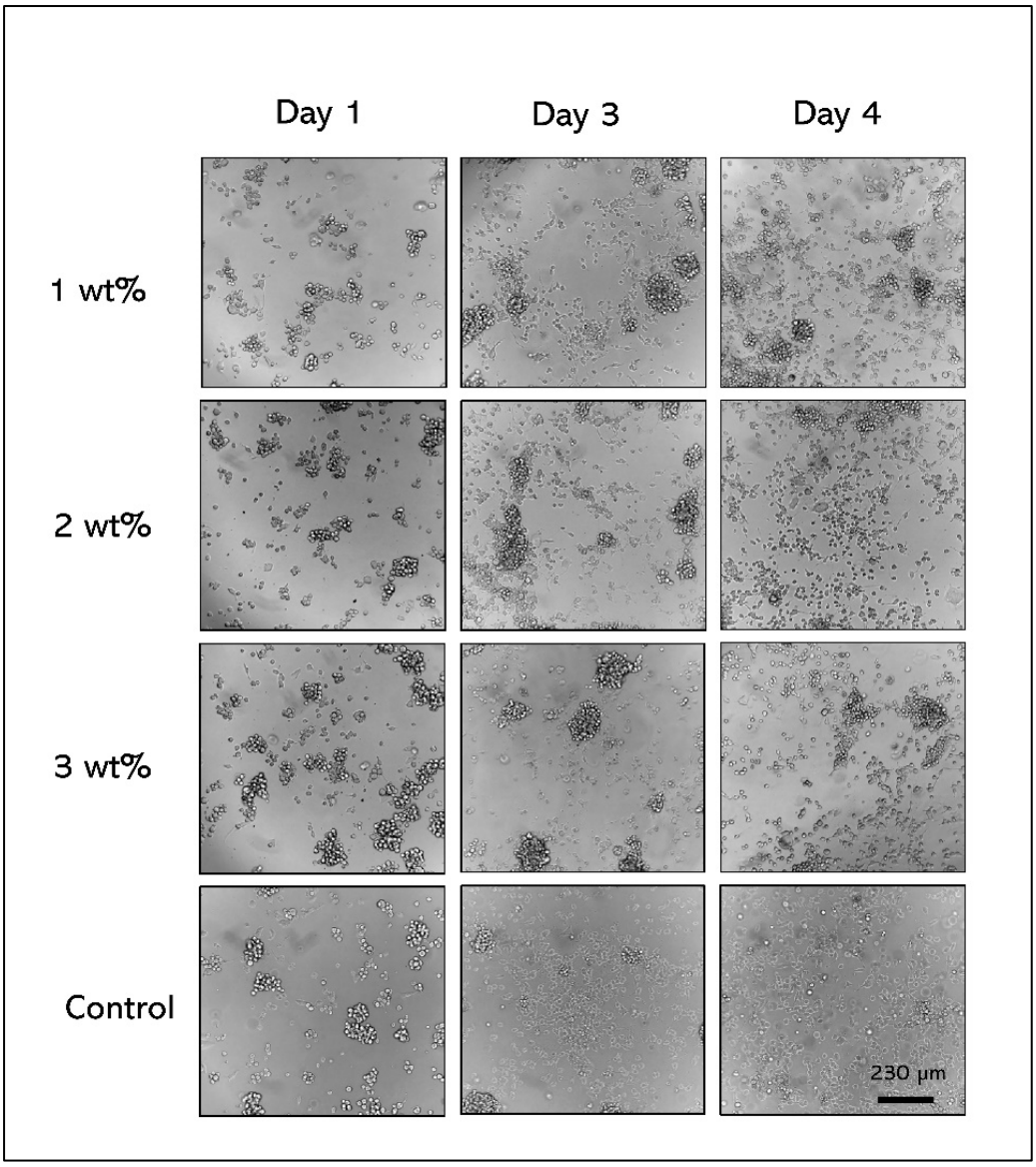

Figure 3.7 Brightfield microscopy images of neuron cells
Scaffolds are printed using 1 wt%, 2 wt% and 3 wt% sodium alginate, and a control sample containing no printed constructed on days 1, 3, and 4. Scale bar = 230 µm. Reprinted with permission (Badr et al., 2022)

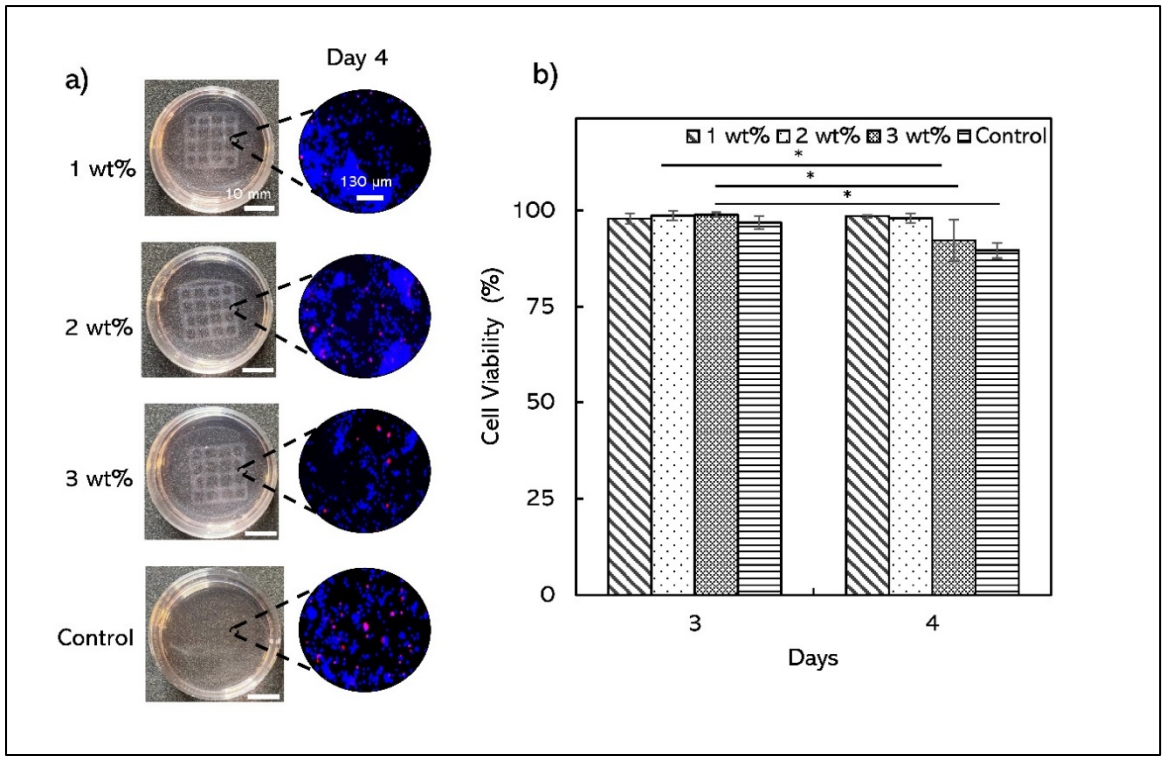

Figure 3.8 Cell viability results
a) Fluorescence images DAPI (blue) and PI (red) for all and dead cells, respectively and b) quantitative cell viability results of Neuro2a cells in 1 wt%, 2 wt%, and 3 wt% sodium alginate on day 4. Scale bar = 130 µm, and single asterisk (*) indicates significant differences between groups ($p < 0.05$). Reprinted with permission (Badr et al., 2022)

CHAPTER 4

A MIST-BASED CROSSLINKING TECHNIQUE FOR COAXIAL BIOPRINTING OF HOLLOW HYDROGEL FIBERS

This chapter includes the results obtained for the development of a mist-based method for coaxial bioprining. The printability, effects of printing parameters on hollow fiber fabrication and dimensions, mechanical properties, and cell viability are assessed. Results presented and discussed in this chapter have been submitted to *Bioprinting*.

4.1 Printability analysis

Scaffolds with various geometries are printed to demonstrate the ability of the system to print single and multi-layer constructs, as shown in Figure 4.1(a-e). Printed filaments are observed under a microscope to confirm that the core mist provides sufficient crosslinking to form a hollow fiber. An example of a printed hollow fiber before and after perfusion is shown in Figure 4.1 (b) and (c), respectively. The 10-layer, 15 × 15 mm construct shown in Figure 4.1(d) demonstrate the ability of the system to print 3D multi-layer geometries, exhibiting good shape fidelity and strong layer adhesion.

As shown in Figure 4.1(e), 2-layer, 30 × 30 mm scaffolds are successfully printed using various concentrations of sodium alginate (2, 3, and 4 wt%) and mist (5, 10, and 20%). Scaffolds printed using core liquid crosslinker (1 wt%) result in the pooling of liquid on the printbed that compromises the shape fidelity of the printed scaffolds (Figure 4.1(e)). The calculated printability values for the printed scaffolds crosslinked using mist are shown in Figure 4.1(f). All scaffolds crosslinked using mist exhibit a printability number within the acceptable range of 0.9-1.1 (Kyle, Jessop, Al-Sabah, & Whitaker, 2017). Through visual inspection, it was observed that scaffolds printed using a high concentration of sodium alginate (4 wt%) and crosslinked with low concentration of mist (5%) collapse post printing due to lack of crosslinking of the inner walls of the hollow fiber. Furthermore, it is visually observed that a high mist concentration (20%) causes rapid gelation and affects layer adhesion, which are

not clearly represented through the printability number. Therefore, it is determined that a mist concentration of 10% is optimal to achieve the required gelation to form a hollow fiber and strong layer adhesion.

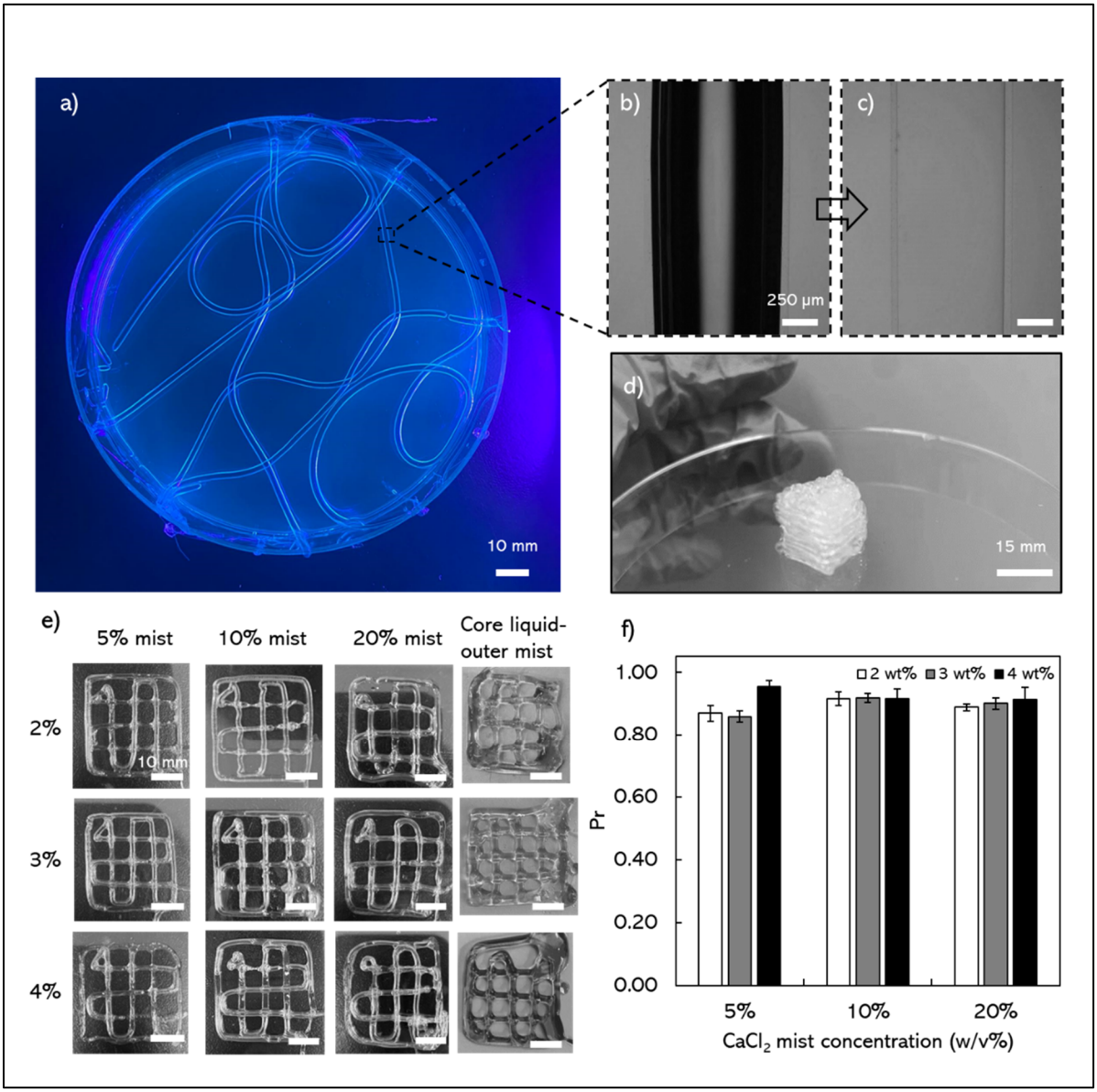

Figure 4.1 Bioprinted hollow fiber constructs
a) Bioprinted hollow fibers. Representative microscopic images of a hollow fiber b) before and c) after perfusion with DI. d) A multi-layer cube printed using 3 wt% alginate and crosslinked with 10% $CaCl_2$ mist. e) 2-layer scaffolds and f) their calculated printability numbers printed using 2, 3 4% wt% sodium alginate and crosslinked with 5, 10, and 20% $CaCl_2$ mist

4.2 Hollow fiber dimensions

Hollow fibers printed using sodium alginate and mist concentrations of 3 wt% and 10%, respectively, are used to determine the effects of the core mist pressure and sodium alginate flowrate on the hollow fiber diameter and wall thickness, as shown in Figure 4.2. Figure 4.2(b,c,d) show the measured diameters and wall thickness of hollow fibers printed using varying core pressures (3.0-6.0 kPa) and sheath flowrates (15, 45 mL/hr). During printing, it is visually observed that a core pressure lower than 3.0 kPa is insufficient to prevent the hollow fiber from collapsing, while a pressure higher than 6.0 kPa results in the splashing of sodium alginate. Results indicate that increasing sodium alginate flowrate and core pressure increase the wall thickness (Figure 4.2(b)) and diameter (Figure 4.2(c,d)), respectively. These results are comparable to previous studies (Gao et al., 2015). It is shown that the core pressure has an observable effect on the formation and uniformity of the hollow fiber; at a high sodium alginate flowrate (45 mL/hr) and a low core pressure of 3.0 kPa, non-uniform fibers are produced, as shown in Figure 4.2(e). The optimal core pressure range is determined to be 4.0-6.0 kPa for sodium alginate flowrates up to 45 mL/hr, as demonstrated in Figure 4.2(e).

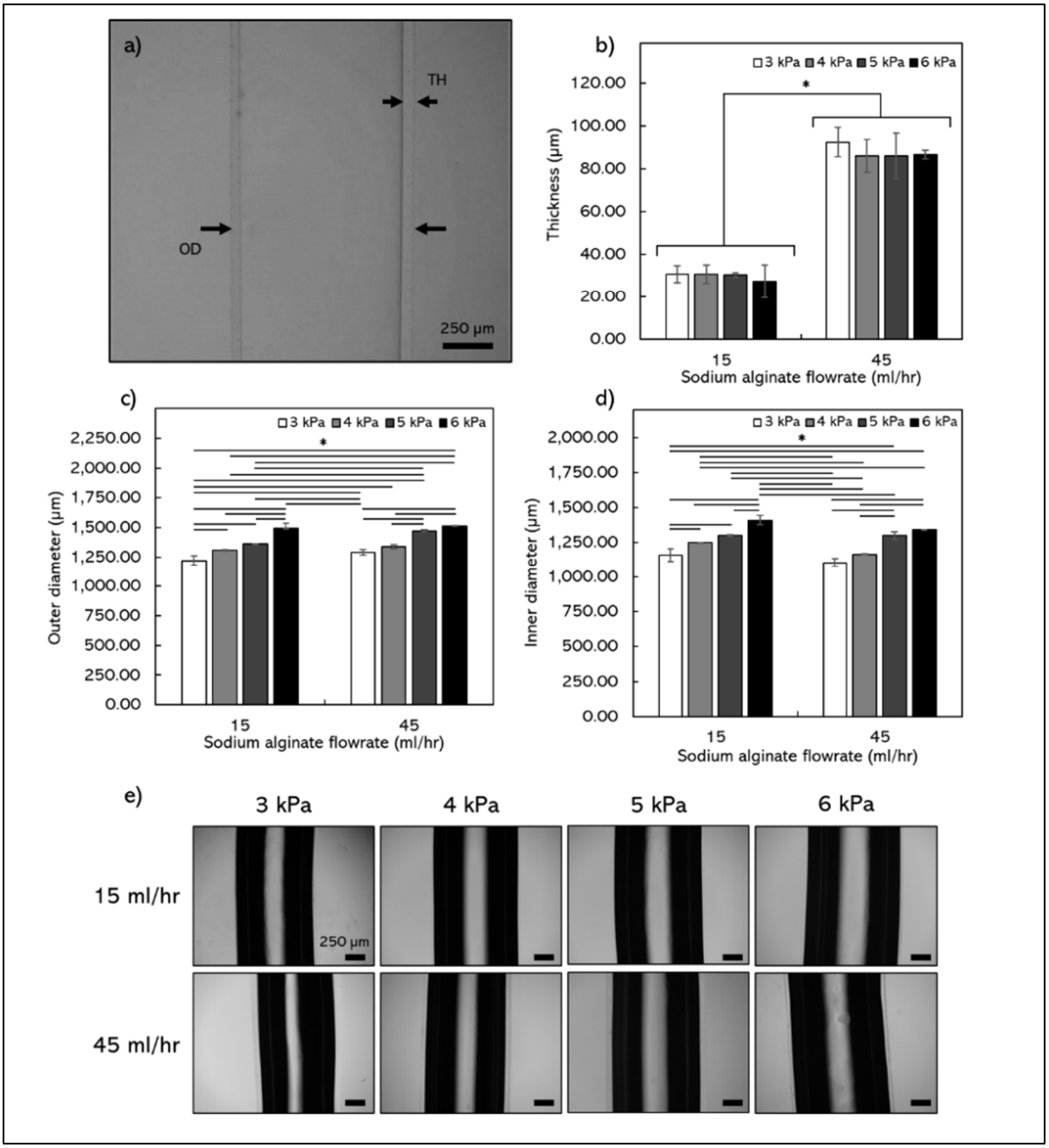

Figure 4.2 Effects of core pressure and sheath flowrate on the fiber diameter and wall thickness

a) An example of a microscopic image used to measure the b) wall thickness, c) outer, and d) inner diameters of hollow fibers fabricated using different mist pressures (3-6 kPa) and sheath flowrates (15, 45 ml/hr). e) Microscopic images of hollow fibers printed using various different mist pressures (3-6 kPa) and sheath flowrates (15, 45 ml/hr). single asterisk (*) indicates significant differences between groups ($p < 0.05$)

4.3 Mechanical characterization

The mechanical properties of 100 mm-long hollow fibers are studied. The breaking strain of the hollow fibers printed using 2, 3, 4 wt% sodium alginate and crosslinked with 5%, 10%, and 20% mist are shown in Figure 4.3. It is shown that both the concentrations of sodium alginate and mist concentration have an impact on the breaking strain of the hollow filaments. It is observed that a higher concentration of alginate leads to a higher breaking strain of the filament (Gong et al., 2016)(Z. Chen et al., 2021). Furthermore, the breaking strain increases as the mist concentration increases, indicating a higher degree of gelation; higher Ca^{2+} concentration promotes additional ionic crosslinks within the hydrogel (J. Chen & Chen, 2020)(Cuadros, Skurtys, & Aguilera, 2012)(Q Wan et al., 2008). Hollow fibers printed using 4 wt% and crosslinked with 20 wt% exhibit the highest breaking strain of 1.06, while fibers printed using 2 wt% and crosslinked with 5 wt% exhibit the lowest strain of 0.32.

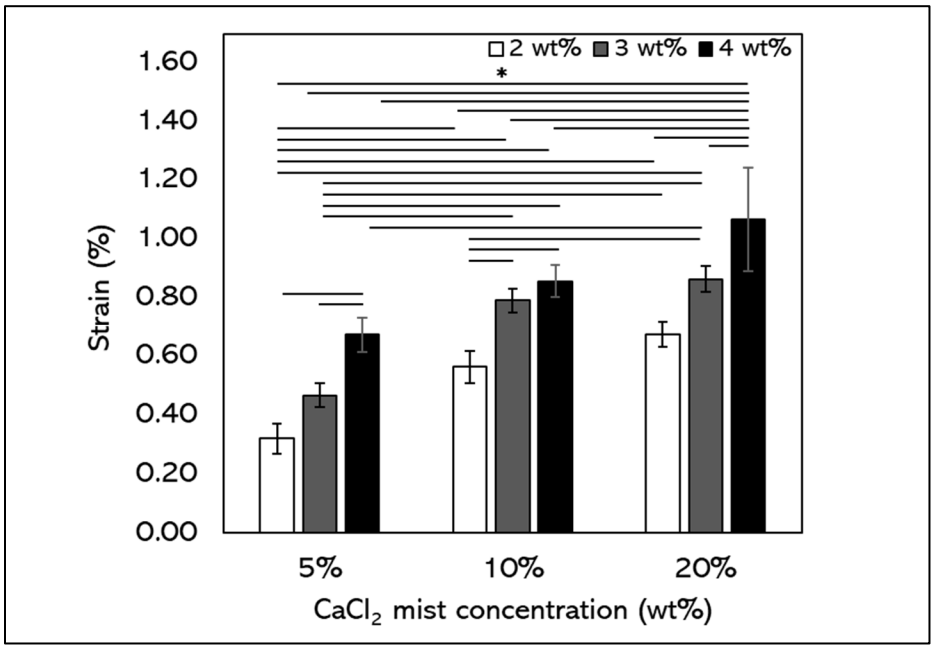

Figure 4.3 Calculated breaking strain of hollow fibers
Hollow fibers printed using 2, 3, and 4 wt% alginates crosslinked with varying $CaCl_2$ mist concentrations (5, 10, 20 wt%). Single asterisk (*) indicates significant differences between groups ($p < 0.05$)

4.4 Cell viability

The viability of Neuro-2a cells seeded on 2-layer, 20 x 20 mm scaffolds printed using 3 wt% sodium alginate and crosslinked in a 1% liquid bath and 10% mist was evaluated. Cells are imaged on days 1, 3 and 7. The brightfield images, overlay of fluorescence images, and quantitative cell viability results are shown inFigure 4.4, Figure 4.5(a), Figure 4.5(b), respectively. The viability values for the control, 10% mist, and liquid bath groups on days 3/7 are 99%/97%, 96%/91%, and 99%/98%, respectively. It is shown that the use of mist (10 wt%) does not affect the cell viability, as no significant differences among the groups are observed on both days 3 and 7. However, on day 7, cell viability of scaffolds crosslinked in a liquid bath is slightly lower than the 10% mist and control groups, suggesting that scaffolds crosslinked in a liquid bath could have a negative effect on the the growth/viability of neuron cells. This could be due to excess Ca^{2+} ions leaching into the cell media and diminishing the cell growth.

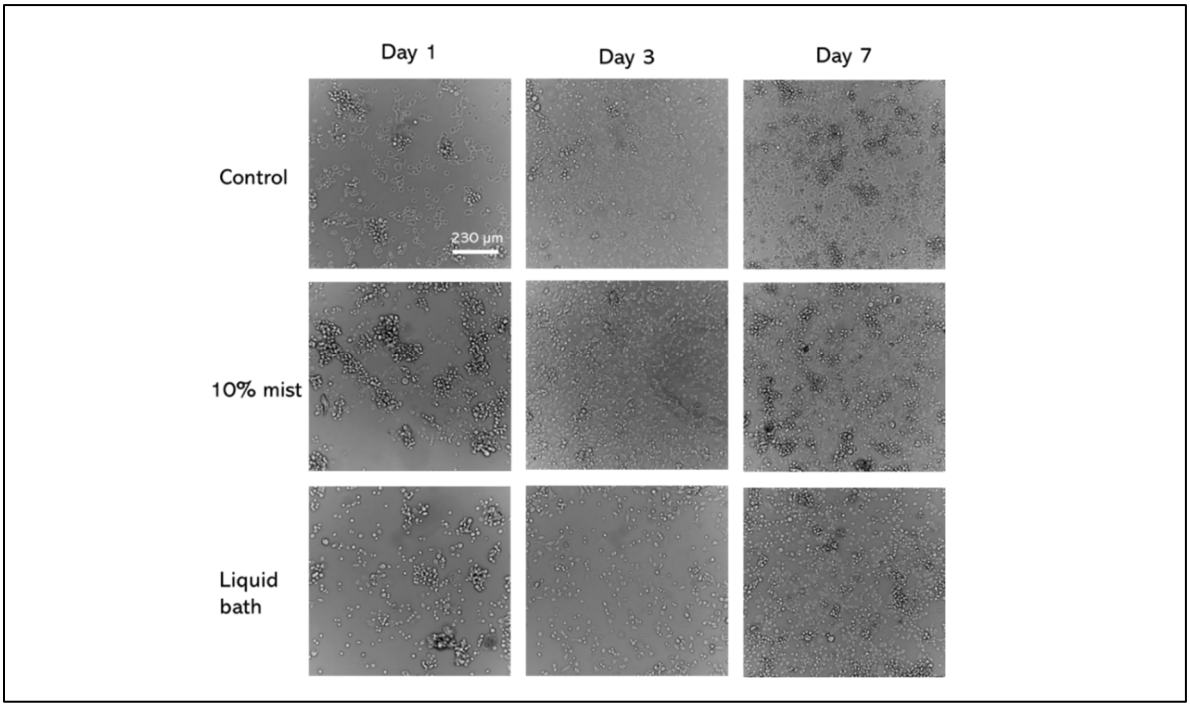

Figure 4.4 Brightfield microscopy images of neuron cells seeded on hollow fibers
Neuron cells are seeded on calcium alginate constructs printed using 3 wt% and crosslinked with 10% mist and in a liquid bath

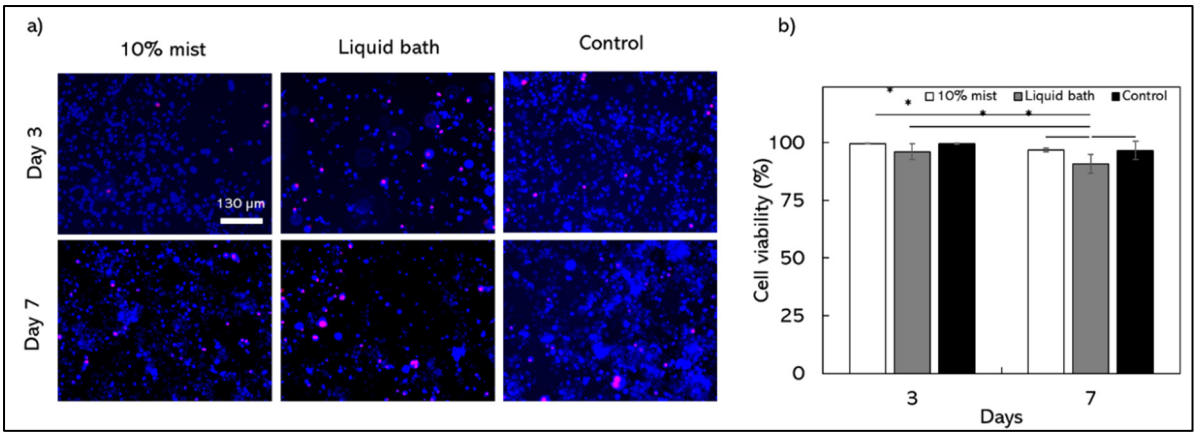

Figure 4.5 Cell viability results
a) DAPI/PI fluorescence images, and b) quantitative cell viability results for Neuro-2a cells seeded on hollow fibers printed using 3 wt% sodium alginate and crosslinked using 10% mist and 1% liquid bath. single asterisk (*) indicates significant differences between groups ($p < 0.05$)

CONCLUSIONS

The developed mist-based crosslinking technologies presented in this thesis leverage the advantages of bioprinting techniques, while providing a better control of the gelation rate and preventing the accumulation of excess crosslinker on the printbed. Furthermore, the developed mist-based technologies advance the applicability of droplet-based and coaxial bioprinting to fabricate complex and biocompatible scaffolds for tissue engineering applications.

The developed mist-based printhead attachment for droplet-based bioprinting delivers the crosslinker in mist form and collects excess crosslinker to prevent the accumulation of crosslinker on the printing stage. Scaffolds printed using sodium alginate crosslinked with mist exhibit good gelation and adhesion between droplets and layers. Additionally, it is shown that increasing the mist flowrate increases the degree of gelation and affects the mechanical properties of the printed constructs. Furthermore, flow simulation results demonstrate that the mist distribution within the printhead is highly dependent on printing parameters such as the inlet flowrate and height from the print stage to the printhead. Moreover, cell viability results demonstrate that printed constructs are biocompatible, suggesting potential for tissue and organ growth using printed scaffolds.

The mist-based coaxial system allows direct printing of continuous and uniform hollow fiber constructs. The use of mist to crosslink the hollow fibers provides better control of the gelation rate, prevents the accumulation of excess crosslinking on the printing substrate, and eliminates the additional post-printing steps that could compromise shape fidelity and cell viability. It is shown that the core pressure has an impact on the formation, uniformity, and dimension of the printed hollow fibers. An optimal core pressure range is determined to achieve uniform, hollow fibers; significantly low core pressures do not provide the adequate support to maintain a hollow tubular structure, while high core pressures result in the splashing of sodium alginate. Furthermore, increasing the core pressure and sodium alginate flowrate result in an increase in the diameter and wall thickness of the hollow fiber, respectively. Additionally, results indicate that increasing the mist concentration increases the degree of crosslinking and thus, affects the

printability and mechanical properties of the hollow fiber structures. A low crosslinker concentration results in the collapsing of the hollow fiber due to lack of crosslinking, while a high crosslinker concentration results in poor layer adhesion due to over-gelation. Therefore, the mist core pressure and concentration are optimized to achieve uniform hollow fiber constructs with strong layer adhesion. Finally, cell viability results show that the scaffolds printed using the mist-based technique are biocompatible with neuron cells, indicating their potential for complex tissue-like structures.

RECOMMENDATIONS

The mist-based technologies have been characterized and optimized for ionically crosslinking hydrogels, particularly sodium alginate; however, the system can be implemented for a wide range of biomaterials and other crosslinking techniques.

Sodium alginate lacks cell-adhesive ligands, and therefore must be modified or combined with other biomaterials. One method of improving sodium alginate's cell adhesion properties is modifying it with cell-adhesive ligands such as arginine-guanidine-aspartate (RGD). Additionally, sodium alginate can be combined with other cell-adhesive hydrogels such collagen, gelatin, or fibrinogen to enable cell attachment and proliferation. Furthermore, crosslinkers such as thrombin or microbial transglutaminase mist could be used to crosslink fibrinogen or gelatin, respectively. To incorporate other hydrogels, the mist-based system must be characterized and optimized through printability, mechanical properties, cell viability, and cell adhesion tests.

The current mist-based system has the potential for further improvement to enable the fabrication of heterogenous tissue structures that better mimic the native tissue. The current system allows the printing of a single hydrogel; however, this could be improved by modifying the printhead to enable the bioprinting of multiple biomaterials to create heterogenous structures. Additionally, the atomizing system can be modified to adjust the crosslinker concentration or flowrate on demand/during the printing process to control the extent of gelation of the printed structures. By controlling the crosslinking concentration, the crosslinking density of the structure can be controlled, and hence, the porosity of the printed structure. This could enable the fabrication of constructs with heterogenous porosity that better mimic native tissue.

APPENDIX I

FLOW SIMULATION OF MIST WITHIN PRINTHEAD

Flow simulation software (Fluent R1, ANSYS) is used to model the mist flow characteristics during printing. The model features a mass flow inlet and pressure outlet for the mist inlet and outlet, respectively. Moreover, the opening to the surroundings at the base of the printhead attachment is modelled as a zero-gauge pressure outlet. Faces within the printhead attachment have a mesh size of 100 μm.

Flow simulation is used to estimate the mist volume fraction in the path of the ejected droplets, thereby demonstrating the effects of key printing parameters on the crosslinking rate, as shown in Figure AI.1.

Figure AI.1(a) shows the calculated mist concentration with respect to the inlet mist flowrate along the path of the ejected droplets. As demonstrated in Figure AI.1(a-i, a-ii, a-iii, a-iv), an increase in mist flowrate results in higher mist concentration within the printhead and, more drastically, between the printhead and print stage. Therefore, increasing the inlet mist flowrate increases the crosslinking rate of the printed droplets. Moreover, a high mist flowrate extends the reach of the mist flow toward the surface of the print stage. To achieve good shape fidelity and co-droplet adhesion, the mist should crosslink the droplets before and after deposition. Therefore, the mist flow should reach the surface of the print stage. The flowrate should be limited, however, to prevent accumulation of liquid crosslinker on the print stage. An inlet flowrate of 1.25 L/min is recommended as it is the lowest flowrate which exhibits an approximately constant mist concentration in the path of the printed droplet, extending to the surface of the print stage.

Figure AI.1(b) shows the calculated mist concentration with respect to the outlet pressure. Similar to the mist inlet flowrate, it is shown that the outlet pressure has a significant effect on the mist concentration within the printhead and between the printhead and print stage:

increasing the pressure reduces the mist concentration. Therefore, the crosslinking rate will diminish as the outlet pressure is increased, resulting in slower crosslinking, although reducing the extent to which mist droplets accumulate on the print stage. The outlet pressure must be selected such that the mist flow reaches the print stage to allow for crosslinking before and after deposition. The highest pressure which exhibits approximately uniform mist concentration along the path of the droplets, 300 Pa, is thereby recommended.

Figure AI.1(c) shows the calculated mist concentration with respect to the gap distance between the printhead and print stage. Figure AI.1(c-i) shows that, with a gap of 2 mm, the mist concentration throughout the path of the printed droplet is the lowest, with increasing concentration shown as the gap distance is increased, as exhibited in Figure AI.1(c-ii) and Figure AI.1(c-iii). It is hypothesized that, as the gap is increased, the mist is removed via the outlet at a slower rate, hence the increase in mist concentration; this is further indicated by lower mist concentrations in the outlet channel as the gap distance is increased. Therefore, the printing height must be high enough such that the mist concentration is uniform along the path of the ejected droplets. The best example of this effect is achieved with a height of 10 mm.

Figure AI.1(d) shows the calculated mist concentration with respect to the diameter of the central channel of the printhead. While the default design features a channel diameter of 4 mm (Figure AI.1(d-ii)), Figure AI.1(d-iii) and Figure AI.1(d-iv) show the resultant mist concentrations when the channel diameter is adjusted to 3 mm and 5 mm, respectively. It is apparent that the mist concentration in the central channel, wherein the printed droplets pass, increases as the channel diameter is decreased. Moreover, a relatively small channel width of 3 mm results in a high concentration of mist in the area above the print stage, suggesting that much of the mist is not collected within the printhead. Conversely, a width of 5 mm results in complete mist collection within the printhead before it reaches the surface of the print stage. Therefore, the channel width must be set to 4 mm.

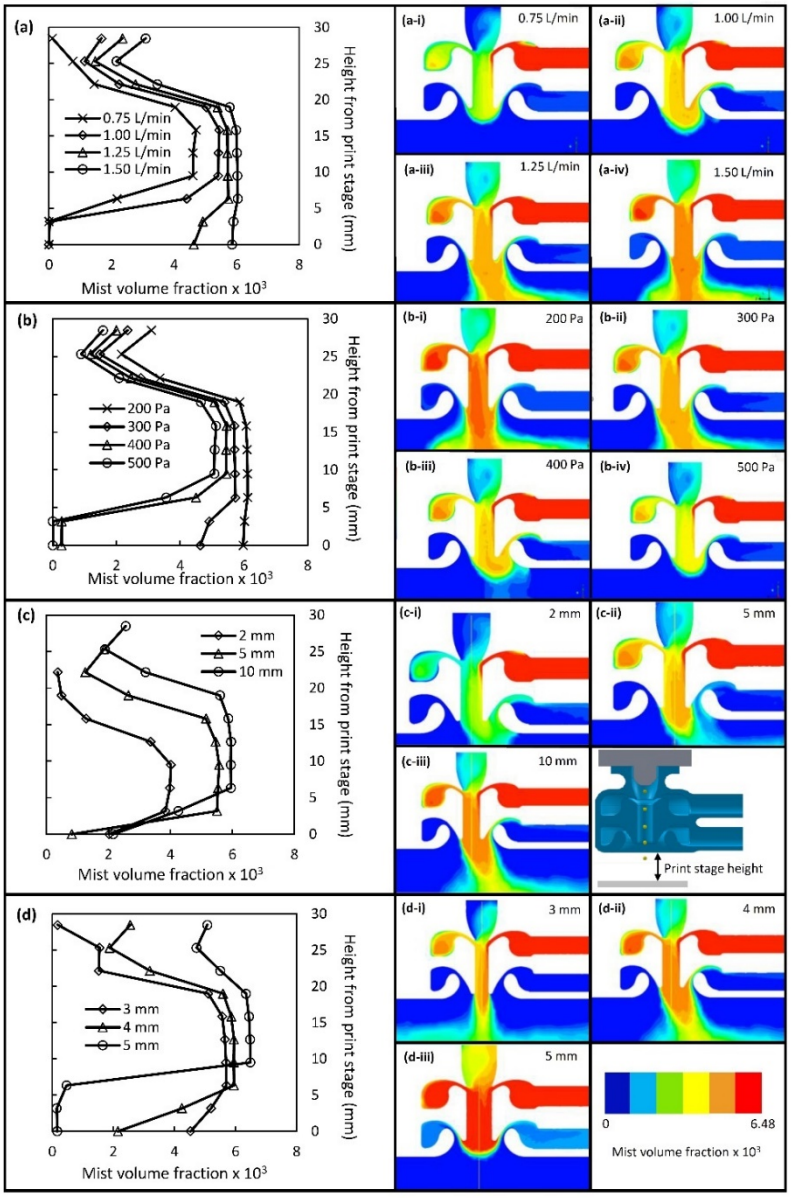

Figure AI.1 Mist distribution flow simulation results within printhead a) Mist concentration with respect to inlet mist flowrate, where the outlet pressure is 300 Pa, print stage height is 5 mm, and diameter of printhead channel is 4 mm. b) Mist concentration with respect to outlet pressure, where the inlet flowrate is 1.25 L/min, print stage height is 5 mm, and diameter of printhead channel is 4 mm. c) Mist concentration with respect to gap distance between printhead and stage, where the inlet flowrate is 1.25 L/min, outlet pressure is 300 Pa, and diameter of printhead channel is 4 mm. d) Mist concentration with respect to diameter of central printhead channel, where the inlet flowrate is 1.25 L/min, outlet pressure is 300 Pa, and print stage height is 5 mm

LIST OF BIBLIOGRAPHICAL REFERENCES

Agarwal, S., Saha, S., Balla, V. K., Pal, A., Barui, A., & Bodhak, S. (2020). Current Developments in 3D Bioprinting for Tissue and Organ Regeneration–A Review. *Frontiers in Mechanical Engineering*, *6*(October). https://doi.org/10.3389/fmech.2020.589171

Aguero, L., Alpdagtas, S., Ilhan, E., Zaldivar-Silva, D., & Gunduz, O. (2021). Functional role of crosslinking in alginate scaffold for drug delivery and tissue engineering: A review. *European Polymer Journal*, *160*(September), 110807. https://doi.org/10.1016/j.eurpolymj.2021.110807

Ahadian, S., & Khademhosseini, A. (2018). A perspective on 3D bioprinting in tissue regeneration. *Bio-Design and Manufacturing*, *1*(3), 157–160. https://doi.org/10.1007/s42242-018-0020-3

Ahmad, Z., Salman, S., Khan, S. A., Amin, A., Rahman, Z. U., Al-Ghamdi, Y. O., … Khan, S. B. (2022). Versatility of Hydrogels: From Synthetic Strategies, Classification, and Properties to Biomedical Applications. *Gels*, *8*(3). https://doi.org/10.3390/gels8030167

Ahn, S., & Kim, G. (2015). Cell-encapsulating alginate microsized beads using an air-assisted atomization process to obtain a cell-laden hybrid scaffold. *Journal of Materials Chemistry B*, *3*(47), 9132–9139. https://doi.org/10.1039/c5tb01629k

Ahn, S., Lee, H., Bonassar, L. J., & Kim, G. (2012). Cells (MC3T3-E1)-laden alginate scaffolds fabricated by a modified solid-freeform fabrication process supplemented with an aerosol spraying. *Biomacromolecules*, *13*(9), 2997–3003. https://doi.org/10.1021/bm3011352

Ashammakhi, N., Ahadian, S., Xu, C., Montazerian, H., Ko, H., Nasiri, R., … Khademhosseini, A. (2019). Bioinks and bioprinting technologies to make heterogeneous and biomimetic tissue constructs. *Materials Today Bio*, *1*(February). https://doi.org/10.1016/j.mtbio.2019.100008

Augst, A. D., Kong, H. J., & Mooney, D. J. (2006). Alginate hydrogels as biomaterials. *Macromolecular Bioscience*, *6*(8), 623–633. https://doi.org/10.1002/mabi.200600069

Badr, S., MacCallum, B., Madadian, E., Kerr, G., Naseri, E., MacDonald, D., … Ahmadi, A. (2022). Development of a mist-based printhead for droplet-based bioprinting of ionically crosslinking hydrogel bioinks. *Bioprinting*, *27*(December 2021), e00207. https://doi.org/10.1016/j.bprint.2022.e00207

Betancourt, N., & Chen, X. (2022). Review of extrusion-based multi-material bioprinting processes. *Bioprinting*, *25*(December 2021), e00189. https://doi.org/10.1016/j.bprint.2021.e00189

Beyer, S. T., Bsoul, A., Ahmadi, A., & Walus, K. (2013). 3D alginate constructs for tissue engineering printed using a coaxial flow focusing microfluidic device. *2013 Transducers and Eurosensors XXVII: The 17th International Conference on Solid-State Sensors, Actuators and Microsystems, TRANSDUCERS and EUROSENSORS 2013*, (June), 1206–1209. https://doi.org/10.1109/Transducers.2013.6626990

Bhattacharjee, T., Zehnder, S. M., Rowe, K. G., Jain, S., Nixon, R. M., Sawyer, W. G., & Angelini, T. E. (2015). Writing in the granular gel medium. *Science Advances*, *1*(8), 1–7. https://doi.org/10.1126/sciadv.1500655

Butler, H. M., Naseri, E., MacDonald, D. S., Andrew Tasker, R., & Ahmadi, A. (2020). Optimization of starch- and chitosan-based bio-inks for 3D bioprinting of scaffolds for neural cell growth. *Materialia*, *12*(January). https://doi.org/10.1016/j.mtla.2020.100737

Cao, H., Duan, L., Zhang, Y., Cao, J., & Zhang, K. (2021). Current hydrogel advances in physicochemical and biological response-driven biomedical application diversity. *Signal Transduction and Targeted Therapy*, *6*(1), 1–31. https://doi.org/10.1038/s41392-021-00830-x

Chen, J., & Chen, M. (2020). *High strength and toughness of double physically cross-linked hydrogels composed of polyvinyl alcohol and calcium alginate*. (August), 1–10. https://doi.org/10.1002/app.49987

Chen, Z., Song, J., Xia, Y., Jiang, Y., Murillo, L. L., Tsigkou, O., … Li, Y. (2021). High strength and strain alginate fibers by a novel wheel spinning technique for knitting stretchable and biocompatible wound-care materials. *Materials Science and Engineering C*, *127*(May), 0–10. https://doi.org/10.1016/j.msec.2021.112204

Christensen, K., Xu, C., Chai, W., Zhang, Z., Fu, J., & Huang, Y. (2015). Freeform inkjet printing of cellular structures with bifurcations. *Biotechnology and Bioengineering*, *112*(5), 1047–1055. https://doi.org/10.1002/bit.25501

Chung, J. H. Y., Naficy, S., Yue, Z., Kapsa, R., Quigley, A., Moulton, S. E., & Wallace, G. G. (2013). Bio-ink properties and printability for extrusion printing living cells. *Biomaterials Science*, *1*(7), 763–773. https://doi.org/10.1039/c3bm00012e

Colosi, C., Costantini, M., Latini, R., Ciccarelli, S., Stampella, A., Barbetta, A., … Dentini, M. (2014). Rapid prototyping of chitosan-coated alginate scaffolds through the use of a 3D fiber deposition technique. *Journal of Materials Chemistry B*, *2*(39), 6779–6791. https://doi.org/10.1039/c4tb00732h

Colosi, C., Shin, S. R., Manoharan, V., Massa, S., Costantini, M., Barbetta, A., … Khademhosseini, A. (2016). Microfluidic Bioprinting of Heterogeneous 3D Tissue Constructs Using Low-Viscosity Bioink. *Advanced Materials*, *28*(4), 677-684a. https://doi.org/10.1002/adma.201503310

Cuadros, T. R., Skurtys, O., & Aguilera, J. M. (2012). Mechanical properties of calcium alginate fibers produced with a microfluidic device. *Carbohydrate Polymers*, *89*(4), 1198–1206. https://doi.org/10.1016/j.carbpol.2012.03.094

Cui X, Boland T, D'Lima DD, L. M. (2012). Thermal Inkjet Printing in Tissue Engineering and Regenerative Medicine. *Recent Pat Drug Deliv Formul*, *6*(2), 149–155.

Datta, P., Ayan, B., & Ozbolat, I. T. (2017). Bioprinting for vascular and vascularized tissue biofabrication. *Acta Biomaterialia*, *51*, 1–20. https://doi.org/10.1016/j.actbio.2017.01.035

de Melo, B. A. G., Jodat, Y. A., Cruz, E. M., Benincasa, J. C., Shin, S. R., & Porcionatto, M. A. (2020). Strategies to use fibrinogen as bioink for 3D bioprinting fibrin-based soft and hard tissues. *Acta Biomaterialia*, *117*, 60–76. https://doi.org/10.1016/j.actbio.2020.09.024

Derakhshanfar, S., Mbeleck, R., Xu, K., Zhang, X., Zhong, W., & Xing, M. (2018). 3D bioprinting for biomedical devices and tissue engineering: A review of recent trends and advances. *Bioactive Materials*, *3*(2), 144–156. https://doi.org/10.1016/j.bioactmat.2017.11.008

Djelveh, G., Gros, J. B., & Bories, B. (1989). An Improvement of the Cell Diffusion Method for the Rapid Determination of Diffusion Constants in Gels or Foods. *Journal of Food Science*, *54*(1), 166–169. https://doi.org/10.1111/j.1365-2621.1989.tb08593.x

Dou, C., Perez, V., Qu, J., Tsin, A., Xu, B., & Li, J. (2021). A State-of-the-Art Review of Laser-Assisted Bioprinting and its Future Research Trends. *ChemBioEng Reviews*, *8*(5), 517–534. https://doi.org/10.1002/cben.202000037

Draget, K. I., & Taylor, C. (2011). Chemical, physical and biological properties of alginates and their biomedical implications. *Food Hydrocolloids*, *25*(2), 251–256. https://doi.org/10.1016/j.foodhyd.2009.10.007

Drury, J. L., & Mooney, D. J. (2003). Hydrogels for tissue engineering: Scaffold design variables and applications. *Biomaterials*, *24*(24), 4337–4351. https://doi.org/10.1016/S0142-9612(03)00340-5

Faulkner-Jones, A., Fyfe, C., Cornelissen, D. J., Gardner, J., King, J., Courtney, A., & Shu, W. (2015). Bioprinting of human pluripotent stem cells and their directed differentiation into hepatocyte-like cells for the generation of mini-livers in 3D. *Biofabrication*, *7*(4). https://doi.org/10.1088/1758-5090/7/4/044102

Galarraga, J. H., Kwon, M. Y., & Burdick, J. A. (2019). 3D bioprinting via an in situ crosslinking technique towards engineering cartilage tissue. *Scientific Reports*, *9*(1), 1–12. https://doi.org/10.1038/s41598-019-56117-3

Gao, Q., He, Y., Fu, J. zhong, Liu, A., & Ma, L. (2015). Coaxial nozzle-assisted 3D bioprinting with built-in microchannels for nutrients delivery. *Biomaterials*, *61*, 203–215. https://doi.org/10.1016/j.biomaterials.2015.05.031

Girón-Hernández, J., Gentile, P., & Benlloch-Tinoco, M. (2021). Impact of heterogeneously crosslinked calcium alginate networks on the encapsulation of β-carotene-loaded beads. *Carbohydrate Polymers*, *271*(March). https://doi.org/10.1016/j.carbpol.2021.118429

Gong, Y., Han, G. T., Zhang, Y. M., Zhang, J. F., Jiang, W., Tao, X. W., & Gao, S. C. (2016). Preparation of alginate membrane for tissue engineering. *Journal of Polymer Engineering*, *36*(4), 363–370. https://doi.org/10.1515/polyeng-2015-0065

Gonzalez-Fernandez, T., Tenorio, A. J., Campbell, K. T., Silva, E. A., & Leach, J. K. (2021). Alginate-Based Bioinks for 3D Bioprinting and Fabrication of Anatomically Accurate Bone Grafts. *Tissue Engineering - Part A*, *27*(17–18), 1168–1181. https://doi.org/10.1089/ten.tea.2020.0305

Grant, G. T., Morris, E. R., Rees, D. A., Smith, P. J. C., & Thom, D. (1973). Biological interactions between polysaccharides and divalent cations: The egg-box model. *FEBS Letters*, *32*(1), 195–198. https://doi.org/10.1016/0014-5793(73)80770-7

Gudapati, H., Dey, M., & Ozbolat, I. (2016). A comprehensive review on droplet-based bioprinting: Past, present and future. *Biomaterials*, *102*, 20–42. https://doi.org/10.1016/j.biomaterials.2016.06.012

Haldar, K., & Chakraborty, S. (2019). Investigation of chemical reaction during sodium alginate drop impact on calcium chloride film. *Physics of Fluids*, *31*(7). https://doi.org/10.1063/1.5100243

Hinton, T. J., Jallerat, Q., Palchesko, R. N., Park, J. H., Grodzicki, M. S., Shue, H. J., … Feinberg, A. W. (2015). Three-dimensional printing of complex biological structures by freeform reversible embedding of suspended hydrogels. *Science Advances*, *1*(9). https://doi.org/10.1126/sciadv.1500758

Hong, J., Yeo, M., Yang, G. H., & Kim, G. (2019). Cell-electrospinning and its application for tissue engineering. *International Journal of Molecular Sciences*, *20*(24). https://doi.org/10.3390/ijms20246208

Hospodiuk, M., Dey, M., Sosnoski, D., & Ozbolat, I. T. (2017). The bioink: A comprehensive review on bioprintable materials. *Biotechnology Advances*, *35*(2), 217–239. https://doi.org/10.1016/j.biotechadv.2016.12.006

Hu, C., Lu, W., Mata, A., Nishinari, K., & Fang, Y. (2021). Ions-induced gelation of alginate: Mechanisms and applications. *International Journal of Biological Macromolecules*, *177*, 578–588. https://doi.org/10.1016/j.ijbiomac.2021.02.086

Hull, S. M., Brunel, L. G., & Heilshorn, S. C. (2022). *3D Bioprinting of Cell-Laden Hydrogels for Improved Biological Functionality*. *2103691*, 1–17. https://doi.org/10.1002/adma.202103691

Imashiro, C., & Shimizu, T. (2021). Fundamental technologies and recent advances of cell-sheet-based tissue engineering. *International Journal of Molecular Sciences*, *22*(1), 1–18. https://doi.org/10.3390/ijms22010425

Jain, P., Kathuria, H., & Dubey, N. (2022). Biomaterials Advances in 3D bioprinting of tissues / organs for regenerative medicine and in-vitro models. *Biomaterials*, *287*(June), 121639. https://doi.org/10.1016/j.biomaterials.2022.121639

Jalaal, M., Seyfert, C., Stoeber, B., & Balmforth, N. J. (2018). Gel-controlled droplet spreading. *Journal of Fluid Mechanics*, *837*, 115–128. https://doi.org/10.1017/jfm.2017.844

Jang, J., Seol, Y. J., Kim, H. J., Kundu, J., Kim, S. W., & Cho, D. W. (2014). Effects of alginate hydrogel cross-linking density on mechanical and biological behaviors for tissue engineering. *Journal of the Mechanical Behavior of Biomedical Materials*, *37*, 69–77. https://doi.org/10.1016/j.jmbbm.2014.05.004

Ji, Y., Yang, Q., Huang, G., Shen, M., Jian, Z., Thoraval, M. J., … Xu, F. (2019). Improved Resolution and Fidelity of Droplet-Based Bioprinting by Upward Ejection. *ACS Biomaterials Science and Engineering*, *5*(8), 4112–4121. https://doi.org/10.1021/acsbiomaterials.9b00400

Kang, H. W., Lee, S. J., Ko, I. K., Kengla, C., Yoo, J. J., & Atala, A. (2016). A 3D bioprinting system to produce human-scale tissue constructs with structural integrity. *Nature Biotechnology*, *34*(3), 312–319. https://doi.org/10.1038/nbt.3413

Karamchand, L., Makeiff, D., Gao, Y., Azyat, K., Serpe, M. J., & Kulka, M. (2023). Bioprinting Biomaterial inks and bioinks for fabricating 3D biomimetic lung tissue : A delicate balancing act between biocompatibility and mechanical printability. *Bioprinting*, *29*(June 2022), e00255. https://doi.org/10.1016/j.bprint.2022.e00255

Khoeini, R., Nosrati, H., Akbarzadeh, A., Eftekhari, A., Kavetskyy, T., Khalilov, R., … Ozbolat, I. T. (2021). Natural and Synthetic Bioinks for 3D Bioprinting. *Advanced NanoBiomed Research*, *1*(8), 2000097. https://doi.org/10.1002/anbr.202000097

Kjar, A., McFarland, B., Mecham, K., Harward, N., & Huang, Y. (2021). Engineering of tissue constructs using coaxial bioprinting. *Bioactive Materials*, *6*(2), 460–471. https://doi.org/10.1016/j.bioactmat.2020.08.020

Kobayashi, J., Kikuchi, A., Aoyagi, T., & Okano, T. (2019). Cell sheet tissue engineering: Cell sheet preparation, harvesting/manipulation, and transplantation. *Journal of Biomedical Materials Research - Part A*, *107*(5), 955–967. https://doi.org/10.1002/jbm.a.36627

Kotlarz, M., Ferreira, A. M., Gentile, P., Russell, S. J., & Dalgarno, K. (2022). Droplet-based bioprinting enables the fabrication of cell–hydrogel–microfibre composite tissue precursors. *Bio-Design and Manufacturing*, *5*(3), 512–528. https://doi.org/10.1007/s42242-022-00192-5

Kyle, S., Jessop, Z. M., Al-Sabah, A., & Whitaker, I. S. (2017). 'Printability'' of Candidate Biomaterials for Extrusion Based 3D Printing: State-of-the-Art.' *Advanced Healthcare Materials*, *6*(16), 1–16. https://doi.org/10.1002/adhm.201700264

Labay, C., Hamouda, I., Tampieri, F., Ginebra, M. P., & Canal, C. (2019). Production of reactive species in alginate hydrogels for cold atmospheric plasma-based therapies. *Scientific Reports*, *9*(1), 1–12. https://doi.org/10.1038/s41598-019-52673-w

Lee, G., Kim, S. J., Chun, H., & Park, J. K. (2021). Multilayered and heterogeneous hydrogel construct printing system with crosslinking aerosol. *Biofabrication*, *13*(4). https://doi.org/10.1088/1758-5090/ac25ca

Lee, K. Y., & Mooney, D. J. (2012). Alginate: Properties and biomedical applications. *Progress in Polymer Science (Oxford)*, *37*(1), 106–126. https://doi.org/10.1016/j.progpolymsci.2011.06.003

Li, S., Jin, J., Zhang, C., Yang, X., Liu, Y., Lei, P., & Hu, Y. (2023). 3D bioprinting vascular networks in suspension baths. *Applied Materials Today*, *30*(October 2022), 101729. https://doi.org/10.1016/j.apmt.2022.101729

Li, X., Liu, B., Pei, B., Chen, J., Zhou, D., Peng, J., … Xu, T. (2020). Inkjet Bioprinting of Biomaterials. *Chemical Reviews*, *120*(19), 10793–10833. https://doi.org/10.1021/acs.chemrev.0c00008

Li, Y., Zhu, J., Cheng, H., Li, G., Cho, H., Jiang, M., … Zhang, X. (2021). Developments of Advanced Electrospinning Techniques: A Critical Review. *Advanced Materials Technologies*, *6*(11), 1–29. https://doi.org/10.1002/admt.202100410

Lin, S., Zhao, B., Zou, S., Guo, J., Wei, Z., & Chen, L. (2018). Impact of viscous droplets on different wettable surfaces: Impact phenomena, the maximum spreading factor, spreading time and post-impact oscillation. *Journal of Colloid and Interface Science*, *516*, 86–97. https://doi.org/10.1016/j.jcis.2017.12.086

Liu, W., Zhang, Y. S., Heinrich, M. A., De Ferrari, F., Jang, H. L., Bakht, S. M., … Khademhosseini, A. (2017). Rapid Continuous Multimaterial Extrusion Bioprinting. *Advanced Materials*, *29*(3), 1–8. https://doi.org/10.1002/adma.201604630

López-Marcial, G. R., Zeng, A. Y., Osuna, C., Dennis, J., García, J. M., & O'Connell, G. D. (2018). Agarose-Based Hydrogels as Suitable Bioprinting Materials for Tissue Engineering. *ACS Biomaterials Science and Engineering*, *4*(10), 3610–3616. https://doi.org/10.1021/acsbiomaterials.8b00903

MacCallum, B., Naseri, E., Butler, H., MacNevin, W., Tasker, R. A., & Ahmadi, A. (2020). Development of a 3D bioprinting system using a Co-Flow of calcium chloride mist. *Bioprinting*, (March), e00085. https://doi.org/10.1016/j.bprint.2020.e00085

Melchels, F. P. W., Feijen, J., & Grijpma, D. W. (2010). A review on stereolithography and its applications in biomedical engineering. *Biomaterials*, *31*(24), 6121–6130. https://doi.org/10.1016/j.biomaterials.2010.04.050

Murphy, S. V, & Atala, A. (2014). 3D bioprinting of tissues and organs. *Nature Publishing Group*, *32*(8), 773–785. https://doi.org/10.1038/nbt.2958

Naghieh, S., Karamooz-Ravari, M. R., Sarker, M. D., Karki, E., & Chen, X. (2018). Influence of crosslinking on the mechanical behavior of 3D printed alginate scaffolds: Experimental and numerical approaches. *Journal of the Mechanical Behavior of Biomedical Materials*, *80*(October 2017), 111–118. https://doi.org/10.1016/j.jmbbm.2018.01.034

Ng, W. L., Huang, X., Shkolnikov, V., Goh, G. L., Suntornnond, R., & Yeong, W. Y. (2021). Controlling Droplet Impact Velocity and Droplet Volume: Key Factors to Achieving High Cell Viability in Sub-Nanoliter Droplet-based Bioprinting. *International Journal of Bioprinting*, *8*(1), 1–17. https://doi.org/10.18063/IJB.V8I1.424

Ng, W. L., Lee, J. M., Yeong, W. Y., & Win Naing, M. (2017). Microvalve-based bioprinting-process, bio-inks and applications. *Biomaterials Science*, *5*(4), 632–647. https://doi.org/10.1039/c6bm00861e

Ng, W. L., Lee, J. M., Zhou, M., Chen, Y. W., Lee, K. X. A., Yeong, W. Y., & Shen, Y. F. (2020). Vat polymerization-based bioprinting - process, materials, applications and regulatory challenges. *Biofabrication*, *12*(2). https://doi.org/10.1088/1758-5090/ab6034

O'Brien, F. J. (2011). Biomaterials & scaffolds for tissue engineering. *Materials Today*, *14*(3), 88–95. https://doi.org/10.1016/S1369-7021(11)70058-X

Okubo, N., Qureshi, A. J., Dalgarno, K., Goh, K. L., & Derebail, S. (2019). Cost-effective microvalve-assisted bioprinter for tissue engineering. *Bioprinting*, *13*(July 2018), e00043. https://doi.org/10.1016/j.bprint.2019.e00043

Osidak, E. O., Kozhukhov, V. I., Osidak, M. S., & Domogatsky, S. P. (2020). Collagen as bioink for bioprinting: A comprehensive review. *International Journal of Bioprinting*, *6*(3), 1–10. https://doi.org/10.18063/IJB.V6I3.270

Ouyang, L., Yao, R., Zhao, Y., & Sun, W. (2016). Effect of bioink properties on printability and cell viability for 3D bioplotting of embryonic stem cells. *Biofabrication*, *8*(3). https://doi.org/10.1088/1758-5090/8/3/035020

Ozbolat, I. T., & Hospodiuk, M. (2016). Current advances and future perspectives in extrusion-based bioprinting. *Biomaterials*, *76*, 321–343. https://doi.org/10.1016/j.biomaterials.2015.10.076

Park, J. U., Hardy, M., Kang, S. J., Barton, K., Adair, K., Mukhopadhyay, D. K., … Rogers, J. A. (2007). High-resolution electrohydrodynamic jet printing. *Nature Materials*, *6*(10), 782–789. https://doi.org/10.1038/nmat1974

Piras, C. C., & Smith, D. K. (2020). Multicomponent polysaccharide alginate-based bioinks. *Journal of Materials Chemistry B*, *8*(36), 8171–8188. https://doi.org/10.1039/d0tb01005g

Q Wan, L., Jiang, J., Arnold, D., Guo, E. X. E., Lu, H. H., & Mow, V. C. (2008). Calcium Concentration Effects on the Mechanical and Biochemical Properties of Chondrocyte-Alginate Constructs. *Cell Mol Bioeng.*, *1*(1), 93–102. https://doi.org/10.1007/s12195-008-0014-x.Calcium

Raddatz, L., Lavrentieva, A., Pepelanova, I., Bahnemann, J., Geier, D., Becker, T., … Beutel, S. (2018). Development and application of an additively manufactured calcium chloride nebulizer for alginate 3D-bioprinting purposes. *Journal of Functional Biomaterials*, *9*(4). https://doi.org/10.3390/jfb9040063

Ravanbakhsh, H., Karamzadeh, V., Bao, G., Mongeau, L., Juncker, D., & Zhang, Y. S. (2021). Emerging Technologies in Multi-Material Bioprinting. *Advanced Materials*, *33*(49), 1–38. https://doi.org/10.1002/adma.202104730

Restan Perez, M., Sharma, R., Masri, N. Z., & Willerth, S. M. (2021). 3D Bioprinting Mesenchymal Stem Cell-Derived Neural Tissues Using a Fibrin-Based Bioink. *Biomolecules*, *11*(8), 1–15. https://doi.org/10.3390/biom11081250

Sakai, S., Ueda, K., Gantumur, E., Taya, M., & Nakamura, M. (2018). Drop-On-Drop Multimaterial 3D Bioprinting Realized by Peroxidase-Mediated Cross-Linking. *Macromolecular Rapid Communications*, *39*(3), 1–6. https://doi.org/10.1002/marc.201700534

Sakurada, S., Sole-Gras, M., Christensen, K., Wallace, D. B., & Huang, Y. (2020). Liquid-absorbing system-assisted intersecting jets printing of soft structures from reactive biomaterials. *Additive Manufacturing*, *31*(August 2019), 100934. https://doi.org/10.1016/j.addma.2019.100934

Sarrigiannidis, S. O., Rey, J. M., Dobre, O., González-García, C., Dalby, M. J., & Salmeron-Sanchez, M. (2021). A tough act to follow: collagen hydrogel modifications to improve mechanical and growth factor loading capabilities. *Materials Today Bio*, *10*(November 2020). https://doi.org/10.1016/j.mtbio.2021.100098

Sharma, C., Dinda, A. K., Potdar, P. D., Chou, C. F., & Mishra, N. C. (2016). Fabrication and characterization of novel nano-biocomposite scaffold of chitosan-gelatin-alginate-hydroxyapatite for bone tissue engineering. *Materials Science and Engineering C*, *64*, 416–427. https://doi.org/10.1016/j.msec.2016.03.060

Shiwarski, D. J., Hudson, A. R., Tashman, J. W., & Feinberg, A. W. (2021). Emergence of FRESH 3D printing as a platform for advanced tissue biofabrication. *APL Bioengineering*, *5*(1). https://doi.org/10.1063/5.0032777

Tabriz, A. G., Hermida, M. A., Leslie, N. R., & Shu, W. (2015). Three-dimensional bioprinting of complex cell laden alginate hydrogel structures. *Biofabrication*, *7*(4). https://doi.org/10.1088/1758-5090/7/4/045012

Taghizadeh, M., Taghizadeh, A., Yazdi, M. K., Zarrintaj, P., Stadler, F. J., Ramsey, J. D., … Schubert, U. S. (2022). Chitosan-based inks for 3D printing and bioprinting. *Green Chemistry*, *24*(1), 62–101. https://doi.org/10.1039/d1gc01799c

Takagi, D., Lin, W., Matsumoto, T., Yaginuma, H., Hemmi, N., Hatada, S., & Seo, M. (2019). High-precision three-dimensional inkjet technology for live cell bioprinting. *International Journal of Bioprinting*, *5*(2), 27–38. https://doi.org/10.18063/ijb.v5i2.208

Tong, A., & Voronov, R. (2022). A Minireview of Microfluidic Scaffold Materials in Tissue Engineering. *Frontiers in Molecular Biosciences*, *8*(January), 1–8. https://doi.org/10.3389/fmolb.2021.783268

Unagolla, J. M., & Jayasuriya, A. C. (2020). Hydrogel-based 3D bioprinting: A comprehensive review on cell-laden hydrogels, bioink formulations, and future perspectives. *Applied Materials Today*, *18*(xxxx), 100479. https://doi.org/10.1016/j.apmt.2019.100479

Vacanti, R. L. and J. P. (1993). Tissue Engineering. *Science*, *260*(5110), 920–926. https://doi.org/10.1080/00131725009342110

Wang, N., Adams, G., Buttery, L., Falcone, F. H., & Stolnik, S. (2009). Alginate encapsulation technology supports embryonic stem cells differentiation into insulin-producing cells. *Journal of Biotechnology*, *144*(4), 304–312. https://doi.org/10.1016/j.jbiotec.2009.08.008

Wang, X., Ao, Q., Tian, X., Fan, J., Tong, H., Hou, W., & Bai, S. (2017). Gelatin-based hydrogels for organ 3D bioprinting. *Polymers*, *9*(9). https://doi.org/10.3390/polym9090401

Weigel, N., Li, Y., Fery, A., & Thiele, J. (2023). From microfluidics to hierarchical hydrogael materials. *Current Opinion in Colloid & Interface Science*, *64*, 101673. https://doi.org/10.1016/j.cocis.2022.101673

Werner, S. R. L., Jones, J. R., Paterson, A. H. J., Archer, R. H., & Pearce, D. L. (2007). Droplet impact and spreading: Droplet formulation effects. *Chemical Engineering Science*, *62*(9), 2336–2345. https://doi.org/10.1016/j.ces.2006.12.024

Westwater, J. W., & Drickamer, H. G. (1975). The Mathematics of Diffusion. In *Journal of the American Chemical Society* (Vol. 79). https://doi.org/10.1021/ja01562a072

Wijshoff, H. (2010). The dynamics of the piezo inkjet printhead operation. *Physics Reports*, *491*(4–5), 77–177. https://doi.org/10.1016/j.physrep.2010.03.003

Wüst, S., Godla, M. E., Müller, R., & Hofmann, S. (2014). Tunable hydrogel composite with two-step processing in combination with innovative hardware upgrade for cell-based three-dimensional bioprinting. *Acta Biomaterialia*, *10*(2), 630–640. https://doi.org/10.1016/j.actbio.2013.10.016

Xu, F., Dawson, C., Lamb, M., Mueller, E., Stefanek, E., Akbari, M., & Hoare, T. (2022). Hydrogels for Tissue Engineering: Addressing Key Design Needs Toward Clinical Translation. *Frontiers in Bioengineering and Biotechnology*, *10*(May). https://doi.org/10.3389/fbioe.2022.849831

Xu, T., Zhao, W., Zhu, J. M., Albanna, M. Z., Yoo, J. J., & Atala, A. (2013). Complex heterogeneous tissue constructs containing multiple cell types prepared by inkjet printing technology. *Biomaterials*, *34*(1), 130–139. https://doi.org/10.1016/j.biomaterials.2012.09.035

Yang, X., Lu, Z., Wu, H., Li, W., Zheng, L., & Zhao, J. (2018). Collagen-alginate as bioink for three-dimensional (3D) cell printing based cartilage tissue engineering. *Materials Science and Engineering C*, *83*(June 2017), 195–201. https://doi.org/10.1016/j.msec.2017.09.002

Ying, G., Jiang, N., Yu, C., & Zhang, Y. S. (2018). Three-dimensional bioprinting of gelatin methacryloyl (GelMA). *Bio-Design and Manufacturing*, *1*(4), 215–224. https://doi.org/10.1007/s42242-018-0028-8

Yoon, S., Park, J. A., Lee, H. R., Yoon, W. H., Hwang, D. S., & Jung, S. (2018). Inkjet–Spray Hybrid Printing for 3D Freeform Fabrication of Multilayered Hydrogel Structures. *Advanced Healthcare Materials*, *7*(14), 1–10. https://doi.org/10.1002/adhm.201800050

Zeng, X., Meng, Z., He, J., Mao, M., Li, X., Chen, P., … Li, D. (2022). Embedded bioprinting for designer 3D tissue constructs with complex structural organization. *Acta Biomaterialia*, *140*, 1–22. https://doi.org/10.1016/j.actbio.2021.11.048

Zennifer, A., Manivannan, S., Sethuraman, S., Kumbar, S. G., & Sundaramurthi, D. (2021). 3D bioprinting and photocrosslinking: emerging strategies & future perspectives. *Materials Science and Engineering C*, *134*(September 2021), 112576. https://doi.org/10.1016/j.msec.2021.112576

Zhang, B., Gao, L., Gu, L., Yang, H., Luo, Y., & Ma, L. (2017). High-resolution 3D Bioprinting System for Fabricating Cell-laden Hydrogel Scaffolds with High Cellular Activities. *Procedia CIRP*, *65*, 219–224. https://doi.org/10.1016/j.procir.2017.04.017

Zhang, H., Cheng, J., & Ao, Q. (2021). Preparation of alginate-based biomaterials and their applications in biomedicine. *Marine Drugs*, *19*(5), 1–24. https://doi.org/10.3390/md19050264

Zhang, Y., Yu, Y., Chen, H., & Ozbolat, I. T. (2013). Characterization of printable cellular micro-fluidic channels for tissue engineering. *Biofabrication*, *5*(2). https://doi.org/10.1088/1758-5082/5/2/025004

Zhu, K., Chen, N., Liu, X., Mu, X., Zhang, W., Wang, C., & Zhang, Y. S. (2018). A General Strategy for Extrusion Bioprinting of Bio-Macromolecular Bioinks through Alginate-Templated Dual-Stage Crosslinking. *Macromolecular Bioscience*, *18*(9), 1–8. https://doi.org/10.1002/mabi.201800127